UNIVERSITY
OF TRENTO

DEPARTMENT OF INFORMATION AND COMMUNICATION TECHNOLOGY

38050 Povo – Trento (Italy), Via Sommarive 14
http://www.dit.unitn.it

AN INTEGRATED MULTI-SCALING STRATEGY BASED ON A PARTICLE SWARM ALGORITHM FOR INVERSE SCATTERING PROBLEMS

Massimo Donelli, Gabriele Franceschini, Anna Martini, and Andrea Massa

October 2004

Technical Report DIT-04-081

An Integrated Multi-Scaling Strategy based on a Particle Swarm Algorithm for Inverse Scattering Problems

Massimo Donelli, *Member*, *IEEE*, Gabriele Franceschini, Anna Martini, and Andrea Massa, *Member*, *IEEE*

Department of Information and Communication Technologies,
University of Trento, Via Sommarive 14, I-38050 Trento - Italy
Tel. +39 0461 882057, Fax +39 0461 882093
E-mail: *andrea.massa@ing.unitn.it*,
{*gabriele.franceschini*, *massimo.donelli*, *anna.martini*}*@dit.unitn.it*
Web-page: *http://www.eledia.ing.unitn.it*

An Integrated Multi-Scaling Strategy based on a Particle Swarm Algorithm for Inverse Scattering Problems

Massimo Donelli, Gabriele Franceschini, Anna Martini, and Andrea Massa

Abstract

The application of a multiscale strategy integrated with a stochastic technique to the solution of nonlinear inverse scattering problems is presented. The approach allows for the explicit and easy handling of many difficulties associated with such a problem ranging from ill-conditioning to nonlinearity and false solutions drawback. The choice of a finite dimensional representation for the unknowns, due to the upper bound to the essential dimension of the data, is iteratively accomplished by means of an adaptive multi-resolution model, which offers considerable flexibility for the inclusion of the *a-priori* knowledge and of the knowledge acquired during the iterative steps of the multiscaling process. Even though a suitable representation of the unknowns could limit the local minima problem, the multi-resolution strategy is integrated with a customized stochastic optimizer based on the behavior of a particle swarm (PSO), which allows to prevent that nonlinearity could induce the solution algorithm into false solutions without a large increasing of the overall computational burden. Selected examples are presented by considering a two-dimensional microwave imaging problem so as to illustrate the key features of the integrated stochastic multi-scaling strategy.

Key words:

Inverse Scattering, Microwave Imaging, Multi-Scaling Method, Particle Swarm Optimizer.

1 Introduction

In the past couple of decades, there have been considerable advances in the efficiency, robustness, and efficacy of inversion methods in every fields related to microwave imaging and electromagnetic inverse scattering. The increased interest is evident from the number of journal articles published on this subject, the ever-growing number of sessions organized in major conferences, several books and proceedings that have recently appeared (see [1][2][3] for an informative overview). Such a scenario seems to indicate that inverse scattering continues to be a primary area of research for many academic, governmental, and industrial teams worldwide.

Many advances have been driven by new as well as old applications (see [4] and the references therein), such as geophysical prospecting and remote sensing [5][6], non-destructive testing and evaluation [7][8], and medical imaging [9][10][11][12]. Moreover, inverse scattering techniques have been applied in a large range of data and conditions (e.g., monochromatic, multi-frequency, and transients conditions).

Within this framework, many researches have been focused into improving the robustness towards false solutions and the convergence rate of inversion techniques as well as into addressing the non-uniqueness and ill-conditioning inherent to inverse scattering problems. Ill-conditioning and false solutions are closely related topics, since they are caused by the limited amount of available information on the problem in hand. It is well known (see [13] for an exhaustive and detailed treatment) that the "direct" problem (i.e., the computation of the scattered field from a probed known scatterer) is directed towards a loss of information. Its solution defines a transformation from a physical quantity (the complete description of the scatterer in terms of geometry as well as dielectric features) with a certain information content to another quantity (the scattered field) with a smaller information content. Such an event implies that the "image" (the scattered field) provided by a band-limited system is smoother than the object under test. Therefore, the corresponding inverse scattering problem requires a transition with a gain of information. This

property provides the explanation of the ill-posedness of the inverse problem. In fact, it is ill-posed (and its discretized counterpart turns out to be ill-conditioned) as a consequence of the loss of information intrinsic to the solution of the direct process.

On the other hand, false solutions (i.e., physically unacceptable solutions, but mathematically acceptable) could be easily avoided by taking into account some information (or *a-priori* information) on the behavior of the actual solution.

Then, the "golden rule" for solving an inverse scattering problem is to add some *additional* information to compensate the loss of information of the imaging process. Such a information is defined as *additional* since cannot be derived neither from the scattered field nor from the properties of the mapping between the data and the unknowns space, which describes the imaging process. It comes from other informative sources or from previous information gained on the object.

The most simple form to add information is to mathematically express some expected physical properties of the scatterer and to use such a knowledge explicitly to construct families of approximate solutions. This is the principle of the regularization methods formulated by A. N. Tikhonov and V. Y. Arsenin in [14]. The underlying idea of regularization consists in considering a family of approximate solutions depending on a parameter called *regularization parameter*. For noise-free data, the approximate solutions converge to the actual solution when the regularization parameter tends to zero. Otherwise, one can obtain an optimal approximation of the exact solution for a non-zero value of the regularization parameter. The choice of the value of the *regularization* parameter is a crucial and non-trivial problem. But, unlike linear inverse scattering problems for which well-developed mathematical methods and efficient numerical algorithms are already available, the scientific literature does not provide any simple rule for the optimal choice of the regularization coefficient when nonlinear problems are dealt with [15].

A different approach to restore well-position is to suitably define the dimension of the unknown space by fully exploiting all the available information on the scenario under test. To come to a well-posed problem, the description of the unknown scatterer is supposed

to belong to a finite dimensional space, which dimension is smaller than the essential dimension of data. Such a dimension, because of the analytical nature of the scattering operator, is a known quantity since it depends on the extension of the investigation domain respect to the wavelength [16] and on the characteristics of the multi-view acquisition system [17].

Unfortunately, the choice of a maximum number of retrievable unknowns equal to the essential dimension of the scattered data does not usually fulfill the criterion given in [18] for a suitable representation (in terms of spatial resolution) for both the dielectric profile of the scatterer and the induced electric field. In order to overcome such a mismatching, various strategies based on a multi-resolution expansion of the unknowns have been proposed. These methods define discretization schemes and corresponding basis functions tailored to represent the variety of length scales in the investigation domain (finer scales near the discontinuities and more spatially diffused over the smooth expanses of the scatterer or in the external homogeneous background). Taking advantage of such a kind of expansion, it is possible to distribute in a non-uniform way the unknowns inside the scattering domain. This is the common rational of the multi-resolution-based approaches. The *a-priori* multi-resolution approach [19], owing to *a-priori* considerations on the mathematical nature of the problem and of the intrinsic features exhibited by the class of retrievable functions, associates part of the total number of unknowns to a coarse representation of the whole domain. Moreover, it concentrates the remaining ones in those parts of the region under test where a better resolution can be achieved. Mathematically, the arising problem is solved through the minimization (only once) of a cost function related to the scattering equations wherein the unknowns are represented with the *a-priori* multi-resolution expansion by considering a suitable wavelet transformation.

A similar multi-resolution approach, based on a Daubechies wavelet expansion, is used in [20] to easily manage different kind of prior statistical models on the scenario under test when linear conditions hold. In such a case, regularization is accomplished through a multi-scale prior stochastic model and a statistic tool (based on the use of the relative

error covariance matrix) is adopted to define the space-varying optimal scale for the reconstruction. The arising inverse scattering problem is then recast to the minimization of a two-terms cost function enforcing fidelity to scattering data and the matching with the statistical prior model for the contrast, respectively.

A different approach based on a step-wise refinement procedure is developed by E. Miller in [21] for a nonlinear scattering model. A sequence of different *a-priori* hypothesis tests (i.e., a collection of anomaly configurations) are employed first to localize anomalous behaviors in large areas and then to refine these initial estimates to better characterize the actual structures. The proposed stable coarse-to-fine localization method defines a decomposition procedure (able to zoom on strong scatterers before refining other structures) and a pruning step to remove unreliable candidate anomalies from further processing.

In the framework of *adaptive* multi-resolution approaches, Caorsi *et al.* proposed in [22] an iterative technique where the distribution of the unknowns is *a-posteriori* determined on the basis of the previous experience about the possible objects to be reconstructed, but avoiding any *a-priori* assumption on the position as well as on the kind of unknown scatterers. The approach takes advantage of a constant multi-scaling piece-wise pulse representation able to deal with all possible multi-resolution combinations (unlike wavelet expansion) and it is aimed at determining firstly the regions-of-interest (RoIs) where the scatterers are located and successively at retrieving quantitative information. The reconstruction process is developed as a sequence of increasingly "finer" representations while at the same time retaining the information achieved in moving from a coarse to a fine scale.

However, unlike the linear case, in nonlinear inverse problems, the condition of a number of independent data equal or smaller than the number of retrievable unknowns may not suffice to reach a reliable inversion because of the false solutions problem. Certainly, a multi-resolution strategy considerably limits (with respect to standard deterministic methods) the occurrence of local minima in the arising cost function by reducing the search space. But, there is no guarantee of avoiding local minima without a proper initialization

(when deterministic optimizers are used). Consequently, it is needed to integrate the multi-resolution strategy (aimed at preventing the ill-positioning of the inverse scattering problem) with a suitable global optimization procedure able to face the problem of false solutions by taking into account the available *a-priori* information (and, for adaptive processes, of the *step-by-step* acquired information) in a simple and computationally effective manner.

Since false solutions are physically unacceptable solutions, the minimization method is required to possess the following main features to prevent their occurrence:

- Simple and efficient inclusion of the available *a-priori* information (and of the *step-by-step* acquired information) on the physical behavior of the unknown solution;
- Easy and on-line control of the solution quality in order to assure that trial solutions, estimated during the sampling of the search space, are admissible solutions. If the acceptable solution has to belong to a subdomain of the solution space (e.g., when further constraints are imposed), the optimizer should monitor such a property under the action of the operators generating the succession of trial solutions;
- Suitable operators able to fully exploit the information on the solution gained during the minimization and/or arising from the *a-priori* information;
- Operators taking into account any possible link between different solution parameters in order to easily replace non-feasible solutions by newly feasible ones without introducing user-defined penalty functions;

In [23], since the proposed multi-resolution method is not dependent on the minimization algorithm and for simplicity, the authors used a conjugate-gradient approach by considering the optimization procedure as a "*black box*" inside the overall system without satisfying at all or in part the previous requirements. On the contrary, in this paper, the overall reconstruction system is considered. An integrated strategy, aimed at preventing the ill-conditioning of the inverse scattering problem with the multi-scaling expansion of

the unknown profiles and at avoiding the solution be trapped in a false solution through a suitable hill-climbing optimization method based on the PSO [24], is presented and assessed by means of an exhaustive numerical validation. More in detail, the paper is organized as follows. In Section 2, the mathematical model and the geometry of an inverse scattering problem is briefly described by pointing out the main features of such a kind of problems. A suitable integrated strategy to face/limit some of the arising drawbacks is then presented by focusing on the *control level* and the *basic level* of the overall system in Section 3 and Section 4, respectively. Numerical experiments and some comparisons with reference methodologies are presented in Section 5 to validate the proposed strategy. Some brief conclusions follows (Sect. 6).

2 The Inverse Scattering Problem - Mathematical Formulation

The starting point for any microwave imaging approach in the spatial domain are the Fredholm integral equations [25], which model the scattering phenomena relating the internal field $\underline{E}^v_{tot}(\underline{r})$, $v = 1, ..., V$ (v being the index of the vth illumination, by assuming a multi-view acquisition setup [26]) and the object function $\tau(\underline{r})$ ($\tau(\underline{r}) = [\varepsilon_r(\underline{r}) - 1] - j\frac{\sigma(\underline{r})}{2\pi f}$, $\varepsilon_r(\underline{r})$ and $\sigma(\underline{r})$ being the relative dielectric permittivity and the electric conductivity, respectively) to the scattered electric field $\underline{E}^{o,v}_{scatt}(\underline{r})$, $o = 1, ..., O$ (o being the index of the *oth observation* region) and to the incident electric field $\underline{E}^v_{inc}(\underline{r})$, respectively.

For a two-dimensional geometry (by omitting the sub-script z), they assume the following scalar form

$$E^{o,v}_{scatt}(x, y) = -j\frac{k_0^2}{4}\int\int_S \tau(x', y')E^v_{tot}(x', y')H_0^{(2)}(k_0 d)\, dx'dy' \quad (x, y) \notin D \tag{1}$$

$$E^v_{inc}(x, y) = E^v_{tot}(x, y) + j\frac{k_0^2}{4}\int\int_S \tau(x', y')E^v_{tot}(x', y')H_0^{(2)}(k_0 d)\, dx'dy' \quad (x, y) \in D \tag{2}$$

where k_0 is the wave number of the background medium (characterized by a known ob-

ject function value τ_0), $H_0^{(2)}$ is the zero-order second-kind Hankel function, and $d = \sqrt{(x-x')^2+(y-y')^2}$. Moreover, D is the *investigation* domain where the unknown scatterer (defined as a discontinuity in the object function distribution with respect to the background, $D_0 = \{(x,\, y)\ such\ that\ \tau(x,\, y) \neq \tau_0\}$) is assumed to be located.

An imaging process is aimed at retrieving the distribution of $\tau(x, y)$ and of the electric field $E^v_{tot}(x,\, y)$ in the investigation domain $(x,\, y) \in D$ by solving the arising inverse problem. To numerically manage such a problem, a discretized version of (1)-(2) is needed. Generally, such a task is performed by measuring, for each illumination v, the scattered fields at a finite number $m_{(v)} = 1,\, ...,\, M_{(v)}$ of pre-defined locations inside the observation region $(O = 1)$ and by subdividing the investigation domain in N identical square subdomains where the unknown object function $(\tau(x_n,\, y_n),\, n = 1,\, ...,\, N)$ as well as the electric field $(E^v_{tot}(x_n,\, y_n),\, n = 1,\, ...,\, N,\, v = 1, ..., V)$ are assumed to be constant. Thus, the problem unknowns are represented through a linear combination of rectangular basis functions $(B_n(x, y),\, n = 1, ..., N)$ as follows

$$\tau(x,\, y) = \sum_{n=1}^{N} \tau(x_n,\, y_n) B_n\,(x,\, y) \qquad (x,\, y) \in D \tag{3}$$

$$E^v_{tot}(x,\, y) = \sum_{n=1}^{N} E^v_{tot}(x_n,\, y_n) B_n\,(x,\, y) \qquad (x,\, y) \in D \tag{4}$$

and, as a result, the discretized form of (1)-(2) is obtained

$$[E^v_{scatt}] = [G^v_{ext}]\,[\tau]\,[E^v_{tot}] \tag{5}$$

$$[E^v_{inc}] = \{[I] - [G^v_{int}]\,[\tau]\}\,[E^v_{tot}] \tag{6}$$

where $[E^v_{scatt}]$ is an array of the measures collected for the vth view at $M_{(v)}$ measurement points of the observation domain; $[\tau]$ is a $N \times N$ diagonal matrix whose nonzero elements are the values of the object function at the N discretization domains of the investigation domain; $[E^v_{inc}]$, $[E^v_{tot}]$ are two arrays of dimension $N \times 1$ containing the samples of the

total and incident electric field at the positions $(x_n,\, y_n)$, $n = 1,\, ...,\, N$; $[G^v_{int}]$, $[G^v_{ext}]$ are the Green's matrices.

Because of the approximations induced by the finite dimensional discretization of $\tau(x, y)$ and $E^v_{tot}(x,\, y)$ (3)-(4) and the presence of an unavoidable measurement noise, the existence of a solution of the algebraic system (5)-(6) is not ensured and a generalized solution has to be defined as the global minimum of the following cost function Φ[(1)]

$$\Phi(\underline{f}) = \frac{\sum_{v=1}^{V} \left\| \left[E^v_{scatt}\right] - \left[G^v_{ext}\right][\tau]\left[E^v_{tot}\right] \right\|^2}{\sum_{v=1}^{V} \left\| \left[E^v_{scatt}\right] \right\|^2} + \frac{\sum_{v=1}^{V} \left\| \left[E^v_{inc}\right] - \left\{[I] - \left[G^v_{int}\right][\tau]\right\}\left[E^v_{tot}\right] \right\|^2}{\sum_{v=1}^{V} \left\| \left[E^v_{inc}\right] \right\|^2} \tag{7}$$

where the two terms in (7) enforce fidelity to the data in the observation domain ($E^v_{scatt}(x_{m_{(v)}},\, y_{m_{(v)}})$, $(x_{m_{(v)}},\, y_{m_{(v)}}) \notin D$) and in the investigation domain ($E^v_{inc}(x_n,\, y_n)$, $(x_n,\, y_n) \in D$), respectively; $\underline{f} = \{\tau(x_n,\, y_n),\, E^v_{tot}(x_n,\, y_n);\, n = 1, ..., N;\, v = 1, ..., V\} = \{f_j;\, j = 1, ..., J;\, J = N \times V\}$. Usually, the unknown profile of the object function is obtained as the solution of the following nonlinear least square problem

$$\underline{f}_{opt} = arg\left\{min_k\left[\Phi\left(\underline{f}_{(k)}\right)\right]\right\} \tag{8}$$

where $\left\{\underline{f}_{(k)};\, k = 1, ..., K\right\}$ is a sequence of trial solutions (k being the iteration number) iteratively updated (but always considering an unique representation for the unknown profile during the minimization process) by using minimization techniques such as the conjugate-gradient method [27] or stochastic methodologies [29], [30].

Unfortunately, to achieve a suitable spatial resolution in the investigation domain, N should be very large and, in forming the "image" of the investigation domain, one would be requested to solve a large nonlinear optimization problem whose size U (i.e., the number of unknowns) is proportional to the number of pixel N in the region-of-interest (RoI) (in principle the overall investigation domain for a "bare" reconstruction).

(1) $\|\ \|$ indicates the ℓ^2 norm.

Focusing on the dimension of the unknowns space (neglecting just now the nonlinearity problem), it should be pointed out that, for a scatterer of limited spatial extension, the scattered fields are band-limited functions and the dimension of the corresponding finite dimensional space depends on the scatterer extension [16]. Therefore, only a limited number of independent data is actually available and, as a consequence, unless some *a-priori* information is available or some kind of regularization is exploited, only a finite number of unknowns can be actually retrieved. Consequently, unavoidable restrictions on the achievable resolution are enforced.

On the other hand, due to the required (in principle and for a single-step reconstruction process) discretization, it is almost impossible to satisfy the sufficient condition to have no local minima other than the global one [28]. Moreover, a not suitable choice of the unknowns (i.e., an excessively large dimension of the unknowns space as well as an inappropriate representation of the unknowns in terms of basis functions) could imply ill-conditioning besides an increased sensitivity to false solutions.

Consequently, to come to a well-posed/well-conditioned problem and to guarantee that the solution lies in the global minimum of the cost function, some countermeasures are needed. To address the first concern, a suitable multi-resolution strategy, aimed at forcing the dimensionality of the space of the unknowns to a lower value than the essential dimension of data, is considered and a detailed description will be reported in Sect. 3. Moreover, to suitably deal with the nonlinear nature of the functional (7), a customized global optimizer should be used. In fact, unlike the linear case, a number of independent data equal to the number of unknowns may not suffice to achieve an accurate inversion because of the false solution problem [28]. Consequently, an approach based on a new (relatively, for the remote sensing, and especially in the framework of microwave imaging) *multiple-agent* technique is adopted (Sect. 4).

3 The Inversion Strategy: The Iterative Multi-Scaling Approach

The key point of the Iterative Multi-Scaling Approach (IMSA) is the determination of a low-order multiscale representation for the unknowns so as to reduce the complexity of the inversion process and to improve the accuracy in the spatial resolution by "suitably" distributing (i.e., through an automatic refinement procedure) finer scales of the representation in selected RoIs during a sequence of iterative steps.

As far as the representation is concerned, the unknowns are expressed as a twofold summation of shifted and dilated forms of a standard step-like basis function

$$\tau(x,\, y) = \sum_{r=1}^{R(s)} \sum_{n(r)=1}^{N(r)} \tau\left(x_{n(r)},\, y_{n(r)}\right) B_{n(r)}\,(x,\, y) \qquad (x,\, y) \in D \tag{9}$$

$$E^v_{tot}(x,\, y) = \sum_{r=1}^{R(s)} \sum_{n(r)=1}^{N(r)} E^v_{tot}\left(x_{n(r)},\, y_{n(r)}\right) B_{n(r)}\,(x,\, y) \qquad (x,\, y) \in D \tag{10}$$

where r is the resolution index and s is the multi-scaling step index. Such a representation allows to simultaneously take into account a broad spectrum of length scales ranging from low-resolution levels to high-resolution levels. The summation over r ranges from 1, which corresponds to the largest characteristic length scale, to $R(s)$, which corresponds to the smallest basis-function support at the s-th scaling step. For a given level r, $N(r)$ is the number of non-overlapped basis functions centered in the area to be represented at the r-th resolution. Therefore, the terms of small length scale can be concentrated at those regions where the unknowns profile varies more rapidly. Then, to fully exploit the *a-priori* (or iteratively gained) information on the dielectric distribution in the investigation domain, the following adaptive multi-step process is performed:

- *Initialization* $(s = 0)$

  Set the problem unknowns to the free-space configuration ($\tau(x, y) = 0.0$ and $E^v_{tot}(x,\, y) = E^v_{inc}(x,\, y)$);

- *Low-Order Reconstruction* $(s = 1)$

  Minimize $\Phi(\underline{f})$ (7) by assuming a coarse representation for the unknowns $\underline{f}^{(1)} = \{\tau(x_n, y_n), E^v_{tot}(x_n, y_n); n = 1, ..., N\}$ uniformly partitioning $(R(s) = 1)$ the investigation domain D according to the amount of information content of the scattering data [16];

- *Multi-Step Process* $(s = 2, ..., S_{opt})$

  - *RoIs Estimation*

    Define the number $Q^{(s)}$, the locations $(x^{(s)}_{c(q)}, y^{(s)}_{c(q)}, q = 1, ..., Q^{(s)})$, and the extensions $(L^{(s)}_{(q)}, q = 1, ..., Q^{(s)})$ of the RoIs according to the *clustering procedure* described in [23] and perform a noise filtering to eliminate some artifacts in the reconstructed image [31];

  - *Multi-Resolution Expansion* $(s \rightarrow s + 1)$

    Refine the representation of the unknowns by increasing the resolution level in the RoIs $(r = R(s))$.

  - *Multi-Resolution Profile Retrieval*

    Minimize $\Phi(\underline{f}^{(s)})$ (7) by considering the multi-resolution representation for the unknowns (9)-(10), $\underline{f}^{(s)} = \left\{\tau\left(x_{n(r)}, y_{n(r)}\right), E^v_{tot}\left(x_{n(r)}, y_{n(r)}\right); n(r) = 1, ..., N(r); r = 1, ..., R(s)\right\}$, $R(s) = s$, and according to the PSO-based approach (Sect. 4);

  - *Termination Procedure*

    Go to the "*RoIs Estimation*" until a stationary condition on the number of RoIs

    $$\frac{\sum_{\varsigma=1}^{s}\left\{\left|Q^{(s)} - Q^{(\varsigma)}\right|\right\}}{s} < \eta_Q \tag{11}$$

    and on the qualitative reconstruction parameters

$$min_{q=1,..,Q^{(s)}} \left\{ \frac{\left| u_{c(q)}^{(s)} - u_{c(q)}^{(s-1)} \right|}{\left| u_{c(q)}^{(s)} \right|} \times 100 \right\} < \eta_u \qquad u = x_c, y_c, L \tag{12}$$

(η_u, $u = x_c, y_c, L$ being fixed thresholds) is reached ($s = S_{opt}$).

4 The Optimization Approach: The Particle Swarm Algorithm

To develop an integrated system able to avoid the false-solutions problem and to fully exploit (possibly on-line, i.e. at each iteration of the s-th "*Multi-Resolution Profile Retrieval*" phase) all the available *a-priori* and *iteratively-acquired* information by taking advantage of the iterative nature of the multi-scaling process, a conjugate-gradient-based approach (CG) does not seem the optimal choice. Although the reduction of the search space, allowed by the multi-scaling procedure (with a favorable data/unknowns ratio), turns out to be an ideal situation, a CG optimizer could be still trapped in local minima unless a suitable initial guess is available. Moreover, during the minimization, it is not-so-easy to monitor the solution admissibility. In general, such a check is delayed at the end of the minimization process. Therefore, a non-physical solution can be generated, which could represent a worse/wrong starting guess (i.e., a trial solution that does not belong to the attraction basin of the global minimum) for the successive step.

Thus, according to the guidelines briefly summarized in Sect. 1, an optimization based on a multiple-agent stochastic technique called PSO [24][32] is considered as minimization tool. As well as stochastic techniques, one aspect making the PSO very interesting lies in the possibility of easily including some information on the unknowns whenever during the minimization process. Such a feature allows one to restrict the solution search to the acceptance domain by positively affecting the convergence speed of the algorithm. Moreover, the reduced dimension of the solution space of the IMSA does not cause an excessive growth of the processing time.

On the other hand, unlike genetic algorithms (GAs) and other heuristic techniques, PSO presents some interesting features to be exploited in microwave imaging problems, as well:

- The PSO is simpler, both in formulation and computer implementation, than the GA, which considers three-genetic operators (the *selection*, the *crossover*, and the *mutation*). PSO considers one simple operator, that is the *velocity updating*;
- In general, heuristic techniques require a careful tuning of the *control parameters*, which strongly influence the behavior of the optimization method. PSO allows an easier manipulation of the calibration parameters and, even though their optimal values depend on the specific problem, some of these parameters can be set for a large class of problems and problem sizes;
- PSO has a flexible and well-balanced mechanism to enhance the global and local exploration of the search space. Such a feature allows one to overcome the premature convergence (or *stagnation*) and it enhances the search capability of the optimizer;
- PSO generally requires a smaller population size, which turns out in a reduced computational cost of the overall minimization by allowing a reasonable compromise between the computational burden and the minimization reliability.

In order to describe the implementation of the particle swarm algorithm and its integration in the IMSA, let us consider a *swarm* of I particles $P^{(s)} = \left\{ p_i^{(s)};\ i = 1,\ ...,\ I \right\}$ (I being the swarm size). Each member of the swarm $p_i^{(s)}$ is described by defining its position $\underline{f}_i^{(s)}$ in the solution space and its velocity $\underline{g}_i^{(s)}$

$$\underline{g}_i^{(s)} = \left\{ g_{i,j}^{(s)};\ j = 1,\ ...,\ J \right\} \tag{13}$$

in flying the solution space starting from position $\underline{f}_{k,i}^{(s)}$ to $\underline{f}_{k+1,i}^{(s)}$. Then, the following operations are iteratively repeated:

- *Initial Setup* ($k = 0$)

Generate a swarm of I particles $P_{k,i}^{(s)} = \left\{ p_{k,i}^{(s)};\ i = 1,\ ...,\ I \right\}$ and associated positions $\underline{f}_{k,i}^{(s)}$ and velocities $\underline{g}_{k,i}^{(s)}$, $i = 1,\ ...,\ I$ according to the information on the solution acquired at the previous step $s-1$:

$$\underline{f}_{k,i}^{(s)} = \Im \left\{ \underline{f}_{k,i}^{(s-1)} \right\} \qquad i = 1,\ ...\ , I \tag{14}$$

$$\underline{g}_{k,i}^{(s)} = \Im \left\{ \underline{g}_{k,i}^{(s-1)} \right\} \qquad i = 1,\ ...\ , I \tag{15}$$

$\Im$ being the linear operator, which maps the solution/velocity at the $(s-1)$-*th* step with resolution levels defined in the investigation domain at the s-*th* step. Set the value of the control parameter called *inertial weight* w_k.

- *Iterative Minimization Process* $(k = 1,\ ...\ , K)$

  - *Swarm Ranking*

    Calculate the value of the cost function (7) of each individual $p_{k,i}^{(s)}$ in the swarm $\Phi_{k,i}^{(s)} = \Phi\left(\underline{f}_{k,i}^{(s)}\right)$, $i = 1,\ ...,\ I$.

  - *Solution Updating*

    Compare each particle's cost function value to the best fitness that the particle has ever attained at any iteration up to current one, $\Phi\left(\underline{b}_{k-1,i}^{(s)}\right) = min_{h=1,...,k-1}\left\{\Phi_{k,i}^{(s)}\right\}$ and update the *"pbest"* trial solution $\underline{b}_{k,i}^{(s)} = \underline{f}_{k,i}^{(s)}$ if $\Phi\left(\underline{f}_{k,i}^{(s)}\right) < \Phi\left(\underline{b}_{k-1,i}^{(s)}\right)$. Update the optimal "*gbest*" trial solution, $p_{k,opt}^{(s)}$, by modifying its position in the solution space $\underline{t}_k^{(s)} = \underline{f}_{k,opt}^{(s)}$, $\underline{f}_{k,opt}^{(s)} = arg\left\{min_i\left[\Phi\left(\underline{f}_{k,i}^{(s)}\right)\right]\right\}$.

  - *Convergence Check*

    Stop the iterative process when the maximum number of iterations $K^{(s)}$ is achieved or a threshold on the cost function value δ (i.e., $\Phi\left\{\underline{t}_k^{(s)}\right\} \leq \delta$, $k = k_{conv}^{(s)}$) is reached, then set $\underline{f}^{(s)} = \underline{t}_k^{(s)}$.

  - *Velocity Updating*

Starting from the knowledge of $\underline{t}_k^{(s)}$ and $\underline{b}_{k,i}^{(s)}$, modify $\underline{g}_{k,i}^{(s)}$ as follows [24]:

$$g_{k+1,i,j}^{(s)} = w g_{k,i,j}^{(s)} + C_1 r_1 \left\{ b_{k,i,j}^{(s)} - f_{k,i,j}^{(s)} \right\} + C_2 r_2 \left\{ t_{k,j}^{(s)} - f_{k,i,j}^{(s)} \right\} \qquad (16)$$

where r_1 and r_2 are uniform random numbers between 0 and 1; C_1 and C_2 are two positive constants called *acceleration coefficients* [33].

– *Admissibility Check*

To reduce excessively large step sizes in the particle's fly, clamp $\left| g_{k+1,i,j}^{(s)} \right|$ to a specified maximum value $G_j^{(s)}$ (according to the reference literature [32], $G_j^{(s)}$ is set to the dynamic range of the jth dimension defined according to the *a-priori* information). Moreover, to limit the search space of the swarm to the physically admissible solution space, change the sign of $g_{k+1,i,j}^{(s)}$ ("*reflecting wall*" boundary condition [32]) when $f_{k+1,i,j}^{(s)}$ turns out to be out of the physical range.

– *Particle's Position Updating*

Modify the particle's position as follows

$$f_{k+1,i,j}^{(s)} = f_{k,i,j}^{(s)} + g_{k+1,i,j}^{(s)} \qquad j = 1, \ldots, J; \; i = 1, \ldots, I \qquad (17)$$

5 Numerical Validation

The numerical assessment is organized in two-parts. In the first part, the performance of the integrated IMSA-PSO strategy will be firstly examined in a set of test cases, which were previously used to test the IMSA-CG strategy and "bare" approaches. Successively, more complicated scenarios will be considered ranging from synthetic multiple-scatterers geometries as well as real objects probed in a controlled environment.

In comparing the reconstructed distributions with the actual ones, the following measures

of success will be used. The first is a relative error measure over all the pixels in a defined region of the investigation domain

$$\Theta_{(j)} = \sum_{r=1}^{R} \frac{1}{N_{(r)}^{(j)}} \sum_{n_{(r)}=1}^{N_{(r)}^{(j)}} \left\{ \frac{\tau(x_{n_{(r)}}, y_{n_{(r)}}) - \tau^{ref}(x_{n_{(r)}}, y_{n_{(r)}})}{\tau^{ref}(x_{n_{(r)}}, y_{n_{(r)}})} \right\} \times 100 \qquad R = S_{opt} \qquad (18)$$

where $j \Rightarrow tot$ when $(x,\, y) \in D$, $j \Rightarrow int$ when $(x,\, y) \in D_0$, and $j \Rightarrow ext$ when $(x,\, y) \in \{D - D_0\}$; τ and τ^{ref} being the values of the actual and reconstructed object function, respectively.

Moreover, two indices of the achieved qualitative imaging will be evaluated:

$$\rho = \frac{\sqrt{\left[x_{c(S_{opt})} - x_c^{ref}\right]^2 + \left[y_{c(S_{opt})} - y_c^{ref}\right]^2}}{\lambda_0} \qquad (Localization\ Error) \qquad (19)$$

$$\Delta = \left\{ \frac{L_{(S_{opt})} - L_{ref}}{L_{ref}} \right\} \times 100 \qquad (Dimensional\ Error) \qquad (20)$$

Concerning the numerical validation, the first test case (#1) is one of that was earlier treated in [22]. The scattering object, shown in a pictorial grey-level representation in Fig. $1(a)$, consists of a centered square hollow cylinder ($\tau_{in} = 0.0$ and $\tau_{out} = 0.5$) whose dimensions are $L_{in} = 0.8\,\lambda_0$ and $L_{out} = 1.6\,\lambda_0$. The investigation region is a square area $L_D = 2.4\,\lambda_0$ wide, while the measurement region is a circle $R = 1.8\,\lambda_0$ in radius where $M_{(v)} = 21$ equally-spaced receivers are located. The number of views is equal to $V = 4$. To model a realistic environment, a Gaussian-type noise characterized by signal-to-noise ratio (SNR) equal to $30\,dB$ has been added to scattering data. Therefore, to take into account the stochastic nature of the noise, the reported results are the average of the executions of the reconstruction procedure for 10 different independent realizations of the random process generating the noisy scattering data.

As far as the IMSA strategy is concerned, the RoI has been discretized in $N(R) = 36$ square sub-domains ($U = 360$, U being the number of the arising unknowns) and the

maximum number of iterations of the optimization process at the *s-th* step has been fixed to $K^{(s)} = 2000$, $s = 1, ..., S_{opt}$. Concerning the characteristic parameters of the PSO, the following configuration has been assumed after a calibration phase and according to the guidelines in the related literature [32][24]: $w = 0.4$ (constant inertial weight), $C_1 = C_2 = 2.0$ (acceleration terms), $I = 20 \simeq \frac{5}{100}U$ (swarm dimension).

In Fig. 1, the processing results at various steps of the IMSA-PSO procedure are shown. According to the sequence of operations described in Sect. 3, the "*low-order reconstruction*" ($s = 1$) is aimed at performing an inversion by using the same level of spatial resolution in the overall investigation domain ($N(R(s)) = N$). The retrieved profile is shown in Fig. $1(b)$ where the dashed line indicates the contour of the actual object. As it can be observed, the scatterer is non-reliably reconstructed as confirmed by the error figures reported in Tab. I (see for example the value of the dimensional error equal to $\Delta\rfloor_{s=1} = 15.02$). However, from such an reconstruction it is possible to identify the region where the object is located. Thanks to this information and to the improved knowledge of the scatterer under test, the resolution accuracy improves in the successive steps (Fig. $1(c)$ - $s = 2$) until the object is satisfactorily reconstructed at the end of the multi-step process [Fig. $1(d)$]. The final error in estimating the support of the scatterer reduces of about five times ($\frac{\Delta\rfloor_{s=1}}{\Delta\rfloor_{s=S_{opt}=4}} \simeq 4.66$) and the localization errors decreases of two-orders in magnitude ($\frac{\rho\rfloor_{s=1}}{\rho\rfloor_{s=S_{opt}=4}} \simeq 1.38 \times 10^2$). For comparison purposes, let us consider the reconstructed profiles with the IMSA-CG strategy, the CG-based approach and the PSO-based method, respectively (Fig. 2). Concerning the "bare" approaches, it should be pointed out that D has been partitioned in $N = 100$ sub-domains, with a homogeneous grid whose cell side is equal to the finest discretization length of the multiscaling process. Moreover, because of the increased dimension of the search space ($U = 500$), the maximum number of iterations for the minimization process has been fixed to $K_{max} = 6000$.

As can be noted from pictorial representations (Fig. 2) and confirmed by the values of error figures in Tab. II, the IMSA-PSO [Fig. $1(d)$] guarantees a non-negligible improvement in comparison with the IMSA-CG strategy [Fig. $2(a)$] as well as the "bare" approaches

[Figs. 2(b)-(c)]. Such an indication is further assessed by observing Fig. 3, which shows the behaviors of the reconstructions of the object function along a horizontal [$y = 0.0$ - Fig. 3(a)] and a vertical [$x = 0.0$ - Fig. 3(b)] section of the investigation domain together with the ideal profile.

Quantitatively, to better highlight the well-known advantages of multi-resolution strategies over standard approaches, let us consider that $\frac{\rho^{(PSO)}}{\rho^{(IMSA-PSO)}} \simeq 0.90 \times 10^2$, $\frac{\Delta^{(PSO)}}{\Delta^{(IMSA-PSO)}} \simeq 4.0$, and $\frac{\Theta_{tot}^{(PSO)}}{\Theta_{tot}^{(IMSA-PSO)}} \simeq 1.4$. Moreover, the obtained performance confirms the effectiveness of the PSO as nonlinear optimizer compared to a standard conjugate-gradient based approach, but especially the capability of the integrated strategy (IMSA-PSO) to fully exploit and enhance the best features of the optimizer ($\frac{\rho^{(IMSA-CG)}}{\rho^{(IMSA-PSO)}} \simeq 71.42 \frac{\rho^{(CG)}}{\rho^{(PSO)}}$ and $\frac{\Delta^{(IMSA-CG)}}{\Delta^{(IMSA-PSO)}} \simeq 3.09 \frac{\Delta^{(CG)}}{\Delta^{(PSO)}}$).

For completeness, as far as the minimization procedure is concerned, Fig. 4 gives the behavior of the cost function $\Phi\left\{\underline{t}_k^{(s)}\right\}$ versus the increasing number of process iterations. Moreover, to evaluate the computational load of the reconstruction process Tab. III gives the values of some representative parameters: T_k (iteration time), K_{tot} (total number of iterations of the minimization procedure, $K_{tot} = \sum_{s=1}^{S_{opt}} k_{conv}^{(s)}$, $k_{conv}^{(s)}$ being the number of iterations needed to achieve the "convergence" at the sth step of the multi-scaling process), and U. As expected, because of the reduced number of unknowns ($\frac{U^{(PSO)}}{U^{(IMSA-PSO)}} = \frac{U^{(CG)}}{U^{(IMSA-CG)}} \simeq 1.39$), the multi-scaling methodology allows a significant reduction of the computational burden at each iteration ($\frac{T_k^{(PSO)}}{T_k^{(IMSA-PSO)}} \simeq 1.5$ and $\frac{T_k^{(CG)}}{T_k^{(IMSA-CG)}} \simeq 1.8$). Concerning the overall computational load of the IMSA-PSO, it turns out to be of the same order but greater than that of the IMSA-CG. However, the trade-off between the increased computational time and the enhancement of reconstruction accuracy (and the possibility to avoid local minima) seems to be in favor of the IMSA-PSO in such an example ($\frac{C_{tot}^{(IMSA-CG)}}{C_{tot}^{(IMSA-PSO)}} \simeq 1.5$, but $\frac{\rho^{(IMSA-CG)}}{\rho^{(IMSA-PSO)}} \simeq 1.05 \times 10^2$ and $\frac{\Delta^{(IMSA-CG)}}{\Delta^{(IMSA-PSO)}} \simeq 3.62$; $C_{tot} = T_k \times K_{tot}$) as well as (in some test-cases also in a more remarkable way) in the following experiments and examples.

As regards to the same scattering scenario, the second experiment is aimed at assessing the

robustness of the proposed integrated strategy to corrupted scattering data. One of the most desirable features of the IMSA-CG was its stability with respect to the noise, then it is interesting to verify whether such a property is confirmed for the IMSA-PSO. Thus, the retrieval process has been carried out by altering the scattering data with different levels of noise (ranging from $SNR = 30\,dB$ to $SNR = 5\,dB$). The results of such an analysis are reported in Fig. 5 and in Fig 6 in terms of reconstructed profiles and behaviors of the error figures, respectively. As expected, the decreasing of the SNR causes a reduction of the reconstruction accuracy (Fig. 5) and larger errors occur in the qualitative [Figs. $6(d)$-(e)] as well as in the quantitative imaging of the scenario under test [Figs. $6(a)$-(b)]. However, the behaviors of the error figures (especially those related to the qualitative reconstruction, ρ and Δ) further assess the effectiveness of the IMSA-PSO in comparison with other methods.

The second test case (#2) concerns with a similar hollow cylinder configuration, but it considers an off-centered disposition of the scatterer ($x_c^{ref} = y_c^{ref} = -0.2\,\lambda_0$) and different thickness of each layer ($L_{in} = 0.4\,\lambda_0$ and $L_{out} = 1.2\,\lambda_0$), to evaluate the spatial resolution of the stochastic integrated strategy. Let us consider the reconstructions obtained with the IMSA-PSO for the scattering configurations (#1) and (#2), at the same noisy conditions $SNR = 30\,dB$. By comparing Fig. $1(c)$ and Fig. $7(a)$, it can be observed that when the dimensions of the inner cylinder reduce, the quality of the retrieved image decreases and the values of the error figures grow (e.g., $\rho\rfloor_{\#1} = 2.1 \times 10^{-3}$ vs. $\rho\rfloor_{\#2} = 4.1 \times 10^{-2}$, $\Delta\rfloor_{\#1} = 3.22$ vs. $\Delta\rfloor_{\#2} = 7.12$, and $\Theta_{int}\rfloor_{\#1} = 3.01$ vs. $\Theta_{int}\rfloor_{\#2} = 6.82$). However, once again, the IMSA-PSO outperforms the IMSA-CG ($\Theta_{tot}\rfloor_{\#2}^{(IMSA-PSO)} = 4.42$ vs. $\Theta_{tot}\rfloor_{\#2}^{(IMSA-CG)} = 5.96$, $\Theta_{int}\rfloor_{\#2}^{(IMSA-PSO)} = 6.82$ vs. $\Theta_{int}\rfloor_{\#2}^{(IMSA-CG)} = 12.15$, and $\Theta_{ext}\rfloor_{\#2}^{(IMSA-PSO)} = 1.66$ vs. $\Theta_{ext}\rfloor_{\#2}^{(IMSA-CG)} = 4.31$). Such a result is further confirmed by varying the environmental conditions as well and, unless very poor conditions ($SNR \leq 5\,dB$), the reconstructed profiles turn out to be quite close to the reference one and they occupies a large area of the actual distribution [Figs. $7(b)$-(c); Tab. IV].

The next example (#3) deals with another single multi-layer object [Fig. $8(a)$ - $\tau_{in} = 2.0$,

$\tau_{out}0.5$, $L_{in} = 0.4\,\lambda_0$, and $L_{out} = 1.2\,\lambda_0$] to further assess the effectiveness of the approach in retrieving stratified distributions. More in detail, such a test case is representative of a scattering scenario complementary to that described in (#1) and (#2) where the dielectric permittivity grows from the inner to the outer layer. Fig. 8 shows the estimated dielectric profiles for different values of the signal-to-noise ratio. As can be noticed and quantitatively pointed out by the values of error figures (Tab. V), the results clearly indicate that the IMSA-PSO successfully reconstructs the scenario under test by detecting the two-layers of the object whatever the noisy conditions. As expected, the accuracy reduces when the level of the noise increases and the symmetry in the reconstruction tends to disappear as shown in Figs. $8(e)$-(f) and highlighted by the variation in the localization error ($\rho\rfloor_{SNR=20\,dB} = 3.6 \times 10^{-3}$ vs. $\rho\rfloor_{SNR=5\,dB} = 1.3 \times 10^{-1}$).

In order to conclude the numerical assessment with synthetic data, the test case (#4) deals with a multi-scatterers scenario, Fig. $9(a)$. The IMSA already demonstrated its effectiveness in dealing with multiple homogeneous objects [23], thus this example considers a more complex configuration characterized by two hollow square cylinders ($\tau_{(1)} = \tau_{(2)} = 0.5$, $L_{(1)\,in} = L_{(2)\,in} = 0.6\,\lambda_0$, and $L_{(1)\,out} = L_{(2)\,out} = 0.8\,\lambda_0$) located at $x^{ref}_{(1)\,c} = y^{ref}_{(1)\,c} = 0.5\,\lambda_0$ and $x^{ref}_{(2)\,c} = y^{ref}_{(2)\,c} = -0.5\,\lambda_0$, respectively. The SNR has been fixed to $20\,dB$.

Figs. $9(b)$ and $9(c)$ show the results at the convergence of the multi-scaling process when the IMSA-PSO and the IMSA-CG are used, respectively. Whatever the method, two different object are detected and located with an adequate degree of accuracy (Tab. VI). However, the deterministic strategy is not able to retrieve the internal layer of the cylinders. On the contrary, the PSO-based approach faithfully predicts the presence of two-layers in each scatterer as pictorially shown Fig. $9(a)$ and, as a consequence, the error figures related to the reconstruction in the internal regions improve ($\Delta^{(IMSA-PSO)}\big\rfloor_{q=1} = 11.04$ vs. $\Delta^{(IMSA-CG)}\big\rfloor_{q=1} = 31.04$, $\Delta^{(IMSA-PSO)}\big\rfloor_{q=2} = 9.24$ vs. $\Delta^{(IMSA-CG)}\big\rfloor_{q=1} = 31.24$ and $\Theta^{(IMSA-PSO)}_{int}\big\rfloor_{q=1} = 4.21$ vs. $\Theta^{(IMSA-CG)}_{int}\big\rfloor_{q=1} = 8.71$, $\Theta^{(IMSA-PSO)}_{int}\big\rfloor_{q=2} = 3.16$ vs. $\Theta^{(IMSA-CG)}_{int}\big\rfloor_{q=2} = 8.26$).

Finally, the last example of the numerical validation is aimed at assessing the effec-

tiveness of the IMSA-PSO as well as to evaluate the allowed improvement in comparison with IMSA-CG when experimental scattering data are used. Towards this aim, the multiple-frequency angular-diversity bistatic data provided by the Institut Fresnel, Marseille, France [34] has been used. Concerning the experimental setup, it consists of a 2D bistatic measurement system with an emitter placed at a fixed position, while a receiver is rotating with an arm along the vertical cylindrical scatterer under test. The distances between emitter-center and receiver-center are set to $720\,mm \pm 3\,mm$ and $720\,mm \pm 3\,mm$, respectively. The target rotates from 0^o to 350^o in steps of 10^o. The rotation of the receiver is from 60^o to 300^o in steps of 5^o. Obviously, the *aspect-limited* nature of the measurement setup leads to a reduction of the available information. Therefore, all $V = 36$ available views and, for each of them, $M_{(v)} = 49$, $v = 1, ..., V$, have been used for the reconstruction. To focus on the capabilities of the proposed approach, the IMSA-PSO has been applied to a monochromatic dataset ($f = 1\,GHz$), avoiding multi-frequency [35] or frequency-hopping approaches [36]. Moreover, the multiple-objects configuration called "*dielTM_8f.exp*", supposed to lie in a square area of $30 \times 30\,cm^2$, has been managed. The scatterers are two homogeneous dielectric cylinders characterized by an object function $\tau_{(q)} = 2.0 \pm 0.3$, $q = 1, 2$ with circular cross-sections $a = 15\,mm$ in radius and placed about $30\,mm$ from the center of the experimental setup where $\ell = 90\,mm$ is the distance between the centers of the cylinders.

As far as the iterative optimizer is concerned, a small swarm dimension has been assumed (if compared to the dimension of the search space) $\frac{I}{U} \simeq 7.5 \times 10^{-3}$, $U = 2664$, to reduce the overall computational burden ($t_k^{(IMSA-PSO)} = 1.75\,sec$) and to evaluate the effectiveness of the approach in sampling a large search-space with a limited number of agents (i.e., trial solutions). The values of the other control parameters have been maintained unaltered.

Figure 10 shows the evolution of the reconstructed profile during the multi-step procedure [right column - Figs. $10(a)(c)(e)(g)$] when the IMSA-PSO is applied. For comparison purposes, on the left column of the same figure [Figs. $10(b)(d)(f)(h)$], the inversion results with the IMSA-CG at the same steps are reported. The final reconstructions of the two

IMSA-based strategies are given in Fig. 11 where the dielectric distributions achieved by using the "bare" methods are included, as well. As can be seen, the profile retrieved with the PSO-based approach is not satisfactory [Fig. $11(c)$] and it is even worse for the CG-based approach [Figs. $11(d)$]. On the contrary, the resolution accuracy heavily improves when the IMSA-based strategies are used [Figs. $11(a)(b)$]. Because of the hill-climbing nature of the stochastic optimizer, the multi-scaling process of the IMSA-PSO strategy requires more iterations to reach the convergence ($S_{opt}^{(IMSA-PSO)} = 5$ vs. $S_{opt}^{(IMSA-CG)} = 4$; $t_k^{(IMSA-CG)} = 1.33\,sec$), but the final result turns out to be better in terms of shaping as well as homogeneity of the estimated structures.

6 Conclusions

In this paper, an approach to the solution of the nonlinear inverse scattering problem, based upon techniques drawn from the fields of multi-scale modeling and stochastic optimization, has been presented. The problem unknowns have been expressed as a twofold summation of rectangular basis functions, which, adaptively and according to the knowledge gained during a multi-step reconstruction process, fit itself to the various length scales associated with the dielectric distribution in the investigation domain. The inversion scheme is based on an adaptive coarse-to-detailed iterative strategy consisting of a sequence of nonlinear reconstructions performed through a suitable global optimizer. To prevent the problem of false solutions (or local minima of the arising nonlinear cost function) and to fully exploit the so-effective spatial distribution of the unknowns, a customized optimization based on the swarm behavior has been adopted.

A number of numerical tests indicated that the new integrated approach keeps the best features of the multi-scaling process, successfully reconstructing various contrasts and different dielectric distributions. Moreover, thanks to the exploitation of the hill-climbing properties of the stochastic optimizer and a suitable sampling of the search space guided by the multi-scaling strategy, it exhibits additional properties that overcome the IMSA-CG

in terms of reconstruction accuracy and accommodation of the *a-priori* (*acquired*) information without requiring an impracticable computational load and unavailable memory resources.

Acknowledgements

The authors wish to thank E. Vico and C. Pedrazzani for their support. Moreover, they would express their gratitude to Ing. D. Residori for kindly providing some numerical results of computer simulations.

References

[1] Special Issue on "Inverse methods in electromagnetics," *IEEE Trans. Antennas Propagat.*, vol. 29, Mar. 1981.

[2] Special Issue on "Computational wave issues in remote sensing, imaging and target identification, propagation, and inverse scattering," *IEEE Trans. Geosci. Remote Sensing*, vol. 38, part I, Jul. 2000.

[3] Special Issue on "Microwave imaging and inverse scattering techniques," *J. Electromagn. Waves Applicat.*, vol. 17, Apr. 2003.

[4] J. Ch. Bolomey, "Recent European developments in active microwave imaging for industrial, scientific, and medical applications, *IEEE Trans. Microwave Theory Tech.*, vol. 37, pp. 2109-2117, Dec. 1989.

[5] D. Goodman, "Ground penetrating radar simulation in engineering and archeology," *Geophysics*, vol. 59, pp. 224-232, 1994.

[6] A. C. Dubey *et al.*, *Detection technology for mines and minelike targets.* Eds. Orlando, FL, 1995.

[7] J. Ch. Bolomey. *Frontiers in Industrial Process Tomography.* Engineering Foundation, 1995.

[8] J. Ch. Bolomey, "Microwave imaging techniques for NDT and NDE," *Proc. Training Workshop on Advanced Microwave NDT/NDE Techniques*, Supelec/CNRS, Paris, Sept. 7-9, 1999.

[9] A. Franchois, A. Joisel, Ch. Pichot, and J. Ch. Bolomey, "Quantitative microwave imaging with a 2.45 GHz planar microwave camera," *IEEE Trans. Medical Imaging*, vol. 17, pp. 550-561, Aug. 1998.

[10] X. Li, S. K. Davis, S. C. Hagness, D. W. van der Weide, and B. D. Van Veen, "Microwave imaging via space-time beamforming: experimental investigation of tumor detection in multilayer breast phantoms," *IEEE Trans. Microwave Theory Tech.*, vol. 52, pp. 1856-1865, Aug. 2004.

[11] Q. Fang, P. M. Meaney, and K. D. Paulsen, "Microwave imaging reconstruction of tissue property dispersion characteristics utilizing multiple-frequency informatio," *IEEE Trans. Microwave Theory Tech.*, vol. 52, pp. 1866-1875, Aug. 2004.

[12] S. Caorsi, A. Massa, M. Pastorino, and A. Rosani, "Microwave medical imaging: potentialities and limitations of a stochastic optimization technique," *IEEE Trans. Microwave Theory Tech.*, vol. 52, pp. 1908-1916, Aug. 2004.

[13] M. Bertero and P. Boccacci, *Introduction to Inverse Problems in Imaging.* IOP Publishing Ltd, Bristol, 1998.

[14] A. N. Tikhonov and V. Y. Arsenin, *Solutions of Ill-Posed Problems.* Winston/Wiley, Washington, 1977.

[15] H. W. Engl and A. Neubauer, "Convergence rate for Tichonov regularization in finite dimensional subspaces of Hilbert scales," *Proc. Amer. Math. Soc.*, vol. 102, pp. 587-592, 1988.

[16] O. M. Bucci and G. Franceschetti, "On the degrees of freedom of scattered fields," *IEEE Trans. Antennas Propagat.*, vol. 37, pp. 918-926, Jul. 1989.

[17] O. M. Bucci and T. Isernia, "Electromagnetic inverse scattering: Retrievable information and measurement strategies," *Radio Sci.*, vol. 32, pp. 2123-2138, Nov.-Dec. 1997.

[18] J. H. Richmond, "Scattering by a dielectric cylinder of arbitrary cross section shape," *IEEE Trans. Antennas Propagat.*, vol. 13, pp. 334-341, May 1965.

[19] O. M. Bucci, L. Crocco, T. Isernia, and V. Pascazio, "Subsurface inverse scattering problems: Quantifying qualifying and achieving the available information," *IEEE Trans. Geosci. Remote Sensing*, vol. 39, pp. 2527-2537, Nov. 2001.

[20] E. L. Miller and A. Willsky, "A multiscale, statistically based inversion scheme for linearized inverse scattering problems," *IEEE Trans. Geosci. Remote Sensing*, vol. 34, pp. 346-357, Mar. 1996.

[21] E. L. Miller, "Statistically based methods for anomaly characterization in images from observations of scattered fields," *IEEE Trans. Image Processing*, vol. 8, pp. 92-101, Jan. 1999.

[22] S Caorsi, M. Donelli, D. Franceschini, and A. Massa, "A new methodology based on an iterative multiscaling for microwave imaging," *IEEE Trans. Microwave Theory Tech.*, vol. 51, pp. 1162-1173, Apr. 2003.

[23] S Caorsi, M. Donelli, and A. Massa, "Detection, location, and imaging of multiple scatterers by means of the iterative multiscaling method," *IEEE Trans. Microwave Theory Tech.*, vol. 52, pp. 1217-1228, Apr. 2004.

[24] J. Kennedy, R. C. Eberhart, and Y. Shi, *Swarm Intelligence.* San Francisco: Morgan Kaufmann Publishiers, 2001.

[25] D. Colton and R. Krees, *Inverse acoustics and electromagnetic scattering theory.* Berlin, Germany: Springer-Verlag, 1992.

[26] S. Caorsi, G. L. Gragnani, and M. Pastorino, "A multiview microwave imaging system for two- dimensional penetrable objects," *IEEE Trans. Microwave Theory Tech.*, vol. 39, pp. 845-851, May 1991.

[27] H. Harada, D. J. N. Wall, T. T. Takenaka, and T. Tanaka, "Conjugate gradient method applied to inverse scattering problems," *IEEE Trans. Antennas Propagat.*, vol. 43, pp. 784-792, Aug. 1995.

[28] T. Isernia, V. Pascazio, and R. Pierri, "On the local minima in a tomographic imaging technique," *IEEE Trans. Geosci. Remote Sensing*, vol. 39, pp. 1596-1607, Jul. 2001.

[29] S. Caorsi, A. Massa, M. Pastorino, "A computational technique based on a real-coded genetic algorithm for microwave imaging purposes," *IEEE Trans. Geosci. Remote Sensing*, vol. 38, pp. 1697-1708, Jul. 2000.

[30] S-Y. Yang, H-K. Choi, and J-W. Ra, "Reconstruction of a large high-contrast penetrable object by using the genetic and Levenberg-Marquardt algorithms," *Microwave Opt. Technol. Lett.*, vol. 6, pp. 17-21, Sept. 1997.

[31] S. Caorsi, M. Donelli, and A. Massa, "Analysis of the stability and robustness of the iterative multi-scaling approach for microwave imaging applications," *Radio Sci.*, (in press).

[32] J. R. Robinson and Y. Rahmat-Sami, "Particle swarm optimization in electromagnetics," *IEEE Trans. Antennas Propagat.*, vol. 52, pp. 771-778, Mar. 2004.

[33] M. Clerk and J. Kennedy, "The particle swarm-explosion, stability, and convergence in a multidimensional complex space," *IEEE Trans. Evolutionary Comput.*, vol. 6, pp. 58-73, Feb. 2002.

[34] K. Belkebir and M. Saillard, Special section: "Testing Inversion Algorithms against Experimental Data," *Inverse Problems*, vol. 17, pp. 1565-1702, Dec. 2001.

[35] K. Belkebir, R. E. Kleinman, and Ch. Pichot, "Microwave imaging - Location and shape reconstruction from multifrequency scattering data," *IEEE Trans. Microwave Theory Tech.*, vol. 45, pp. 469-476, Apr. 1997.

[36] R. Ferraye, J. Y. Dauvignac, and Ch. Pichot, "An inverse scattering method based on contour deformations by means of a level set method using frequency hopping technique," *IEEE Trans. Antennas Propagat.*, vol. 51, pp. 1100-1113, May 2003.

Figure Captions

- **Figure 1.** Centered hollow square dielectric cylinder ($L_{in} = 0.8\,\lambda_0$, $L_{out} = 1.6\,\lambda_0$, $\tau = 0.5$ - *Noisy Conditions*: $SNR = 30\,dB$) - Actual dielectric distribution (a). Retrieved distributions with the *IMSA-PSO* Strategy at (b) $s = 1$, (c) $s = 2$, and (d) $s = S_{opt} = 4$.

- **Figure 2.** Centered hollow square dielectric cylinder ($L_{in} = 0.8\,\lambda_0$, $L_{out} = 1.6\,\lambda_0$, $\tau = 0.5$ - *Noisy Conditions*: $SNR = 30\,dB$) - Dielectric distributions reconstructed at the convergence by means of (a) the *IMSA-CG* Strategy, (b) the *CG-based* Approach, and (c) the *PSO-based* Approach.

- **Figure 3.** Centered hollow square dielectric cylinder ($L_{in} = 0.8\,\lambda_0$, $L_{out} = 1.6\,\lambda_0$, $\tau = 0.5$ - *Noisy Conditions*: $SNR = 30\,dB$) - Comparison between the retrieved profile and the actual one along the (a) x-axis and the (b) y-axis (*actual profile* - red line; *IMSA-PSO* Strategy - blue line; *IMSA-CG* Strategy - green line; *CG-based* Approach - magenta line; *PSO-based* Approach - light blue line.

- **Figure 4.** Centered hollow square dielectric cylinder ($L_{in} = 0.8\,\lambda_0$, $L_{out} = 1.6\,\lambda_0$, $\tau = 0.5$ - *Noisy Conditions*: $SNR = 30\,dB$) - Behavior of the cost function during the iterative process for the *IMSA-PSO* Strategy, the *IMSA-CG* Strategy, the *CG-based* Approach, and the *PSO-based* Approach.

- **Figure 5.** Centered hollow square dielectric cylinder ($L_{in} = 0.8\,\lambda_0$, $L_{out} = 1.6\,\lambda_0$, $\tau = 0.5$ - *Noisy Conditions*) - Comparison between the dielectric profile reconstructed with the *IMSA-PSO* Strategy and the actual one along the (a) x-axis and the (b) y-axis for different SNR values (*Actual profile* - red line; $SNR = 30\,dB$ - green line; $SNR = 20\,dB$ - blu line; $SNR = 10\,dB$ - magenta line; $SNR = 5\,dB$ - light blue line.

- **Figure 6.** Centered hollow square dielectric cylinder ($L_{in} = 0.8\,\lambda_0$, $L_{out} = 1.6\,\lambda_0$,

$\tau = 0.5$ - *Noisy Conditions*) - Behaviors of the error figures versus SNR values: (a) Θ_{tot}, (b) Θ_{int}, (c) Θ_{ext}, (d) ρ (*Localization* error), and (e) Δ (*Dimensional* error).

- **Figure 7.** Off-centered hollow square cylinder ($L_{in} = 0.4\lambda_0$, $L_{out} = 1.2\lambda_0$, $\tau = 0.5$ - *Noisy Conditions*) - Dielectric distribution retrieved by using the *IMSA-PSO* Strategy when (a) $SNR = 30\,dB$, (b) $SNR = 20\,dB$, (c) $SNR = 10\,dB$, and (d) $SNR = 5\,dB$. Horizontal $(y = 0.0)$ (e) and vertical $(x = 0.0)$ (f) cross-section view.

- **Figure 8.** Centered stratified square dielectric cylinder ($L_{in} = 0.4\,\lambda_0$, $\tau_{in} = 2.0$ and $L_{out} = 1.2\lambda_0$, $\tau_{out} = 0.5$) - (a) Reference distribution. Dielectric distribution retrieved by using the *IMSA-PSO* Strategy when (b) $SNR = 20\,dB$, (c) $SNR = 10\,dB$, and (d) $SNR = 5\,dB$. Horizontal $(y = -0.2\,\lambda_0)$ (e) and vertical $(x = -0.2\,\lambda_0)$ (f) cross-section view.

- **Figure 9.** Multiple off-centered hollow square dielectric cylinders ($\tau_{(1)} = \tau_{(2)} = 0.5$, $L_{(1)\,in} = L_{(2)\,in} = 0.6\,\lambda_0$, and $L_{(1)\,out} = L_{(2)\,out} = 0.8\,\lambda_0$ - *Noisy Conditions*: $SNR = 20\,dB$) - Actual distribution (a). Dielectric distributions retrieved at the convergence by using *(b)* the *IMSA-PSO* Strategy and *(c)* the *IMSA-CG* Strategy.

- **Figure 10.** Multiple circular homogeneous dielectric cylinders ($\tau_{(1)} = \tau_{(2)} = 2.0 \pm 0.3$, $L_{(1)} = L_{(2)} = 30\,mm$, $d = 90\,mm$ - Real dataset "Marseille" [34]) - Retrieved distributions at different steps of the *IMSA* integrated with the *PSO* algorithm (*left*) and the *CG* algorithm (*right*): *(a)*-*(b)* $s = 1$, (c)-(d) $s = 2$, (e)-(f) $s = 3$, and (g)-(h) $s = 4$.

- **Figure 11.** Multiple circular homogeneous dielectric cylinders ($\tau_{(1)} = \tau_{(2)} = 2.0 \pm 0.3$, $L_{(1)} = L_{(2)} = 30\,mm$, $d = 90\,mm$ - Real dataset "Marseille" [34]) - Dielectric distributions reconstructed at the convergence by means of *(a)* the *IMSA-PSO* Strategy ($s = S_{opt} = 5$), *(b)* the *IMSA-CG* Strategy ($s = S_{opt} = 4$), *(c)* the *PSO-based* Approach, and *(d)* the *CG-based* Approach.

Table Captions

- **Table I.** Centered hollow square dielectric cylinder ($L_{in} = 0.8\,\lambda_0$, $L_{out} = 1.6\,\lambda_0$, $\tau = 0.5$ - *Noisy Conditions*: $SNR = 30\,dB$) - Values of the qualitative (ρ and δ) and quantitative (ε_{tot}, ε_{int}, and ε_{ext}) error figures for *IMSA-PSO* Strategy and *IMSA-CG* Strategy at different steps s ($s = 1$, ..., S^{opt}) of the multi-scaling procedure.

- **Table II.** Centered hollow square dielectric cylinder ($L_{in} = 0.8\,\lambda_0$, $L_{out} = 1.6\,\lambda_0$, $\tau = 0.5$ - *Noisy Conditions*: $SNR = 30\,dB$) - Values of the error figures at the convergence for the *IMSA-PSO* Strategy, the *IMSA-CG* Strategy, the *CG-based* Approach, and the *PSO-based* Approach.

- **Table III.** Centered hollow square dielectric cylinder ($L_{in} = 0.8\,\lambda_0$, $L_{out} = 1.6\,\lambda_0$, $\tau = 0.5$ - *Noisy Conditions*: $SNR = 30\,dB$) - Characteristic parameters of the iterative reconstruction process when the *IMSA-PSO* Strategy, the *IMSA-CG* Strategy, the *CG-based* Approach, and the *PSO-based* Approach are used (t_k $[sec]$).

- **Table IV.** Off-centered hollow square dielectric cylinder ($L_{in} = 0.4\,\lambda_0$, $L_{out} = 1.2\,\lambda_0$, $\tau = 0.5$ - *Noisy Conditions*) - Values of the error figures at $s = S^{opt}$ (*IMSA-PSO* Strategy) for different SNRs.

- **Table V.** Reconstruction of a centered stratified square dielectric cylinder ($L_{inner} = 0.4\lambda_0$, $\tau_{inner} = 2.0$ and $L_{outer} = 1.2\lambda_0$, $\tau_{outer} = 0.5$ - *Noisy Conditions*) - Values of the error figures at $s = S^{opt}$ (*IMSA-PSO* Strategy) for different SNRs.

- **Table VI.** Multiple off-centered hollow square dielectric cylinders ($\tau_{(1)} = \tau_{(2)} = 0.5$, $L_{(1)\,in} = L_{(2)\,in} = 0.6\,\lambda_0$, and $L_{(1)\,out} = L_{(2)\,out} = 0.8\,\lambda_0$ - *Noisy Conditions*: $SNR = 20\,dB$) Values of the error figures at the convergence for the *IMSA-PSO* Strategy and the *IMSA-CG* Strategy.

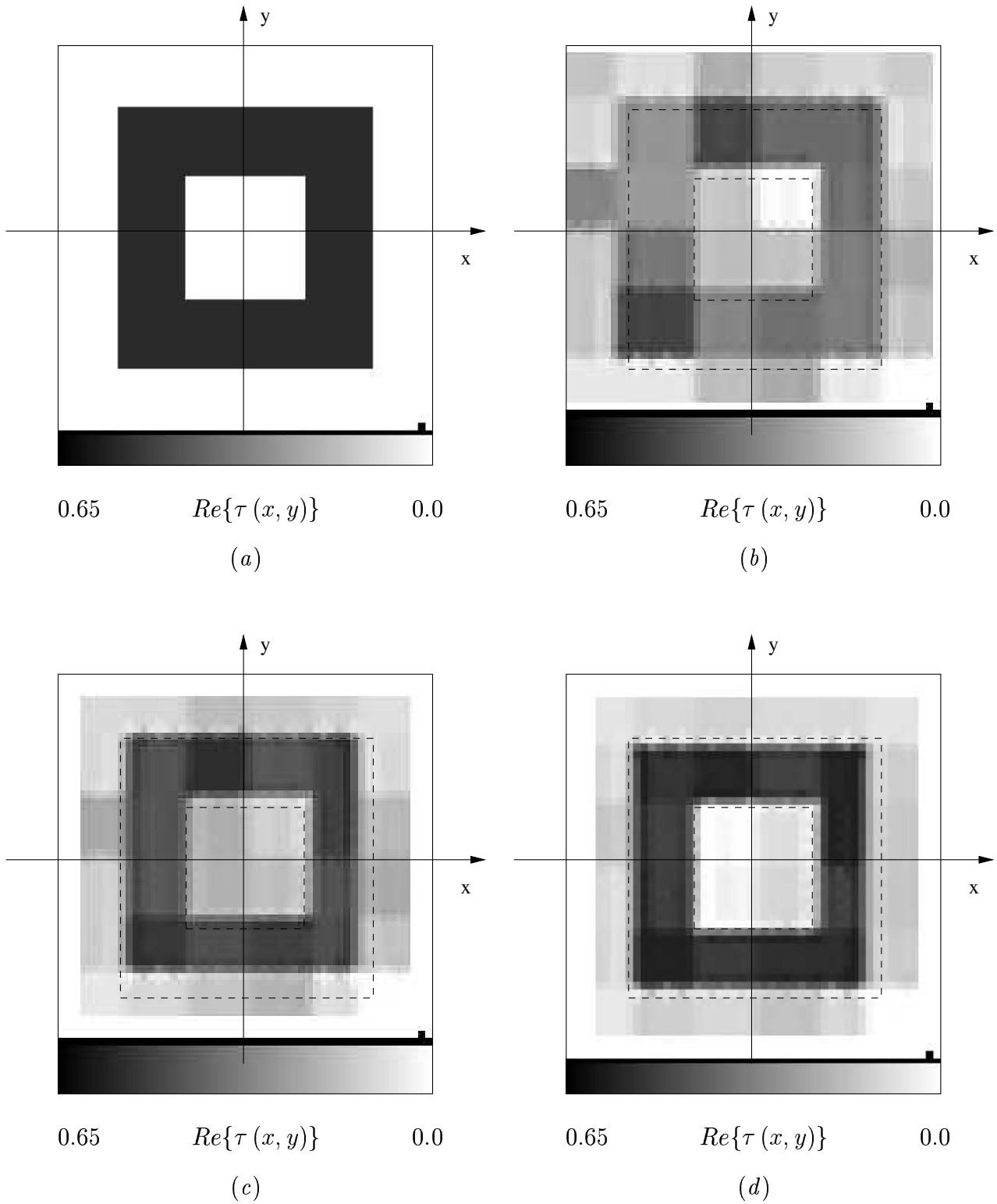

Fig. 1 - M. Donelli *et al.*, "A computational approach based on ..."

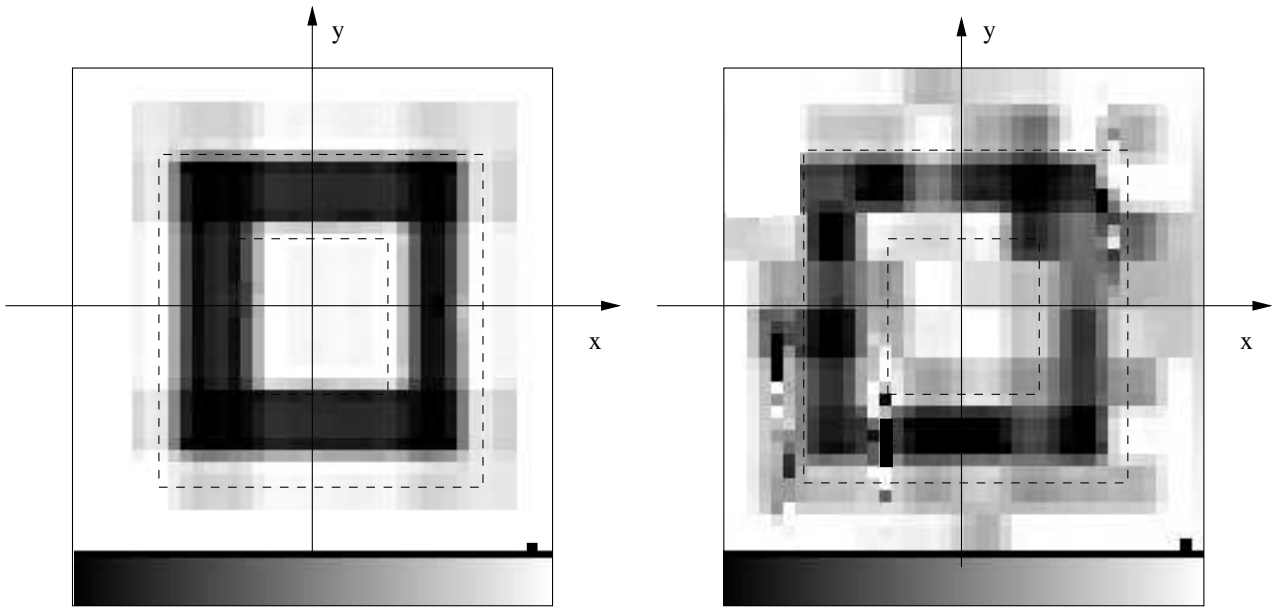

0.65 $Re\{\tau\,(x,y)\}$ 0.0

(a)

0.65 $Re\{\tau\,(x,y)\}$ 0.0

(b)

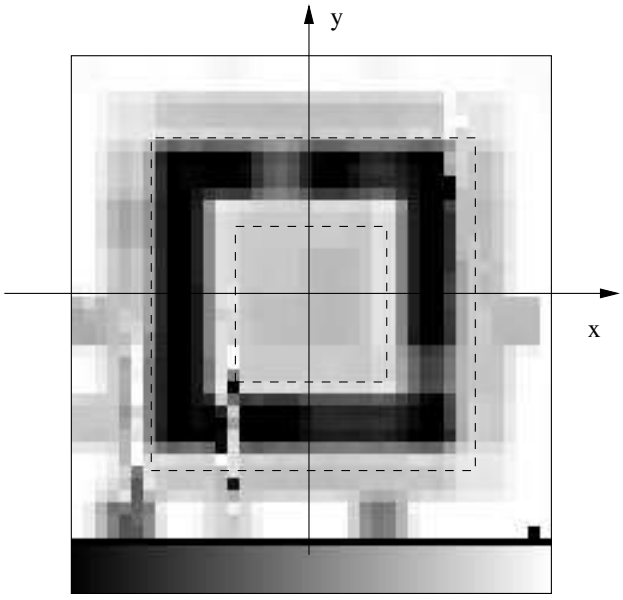

0.65 $Re\{\tau\,(x,y)\}$ 0.0

(c)

Fig. 2 - M. Donelli *et al.*, "A computational approach based on ..."

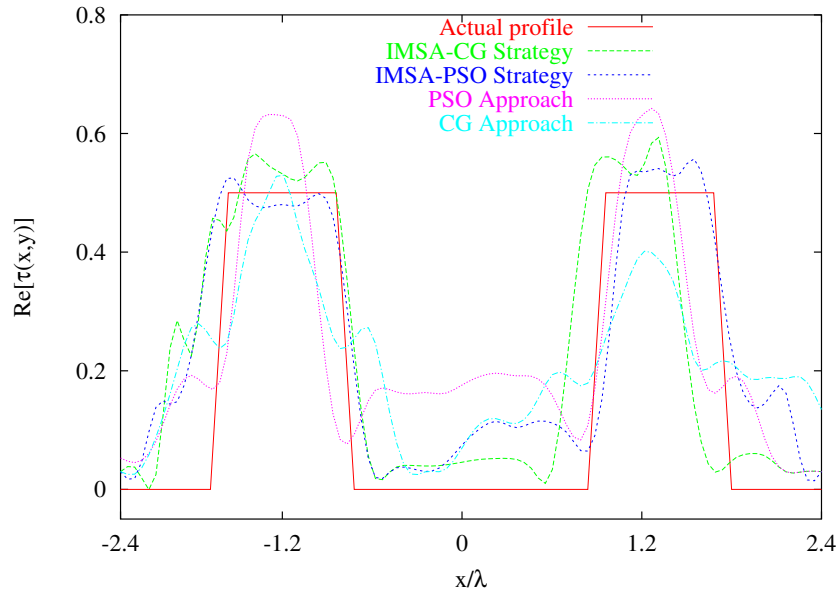

(a)

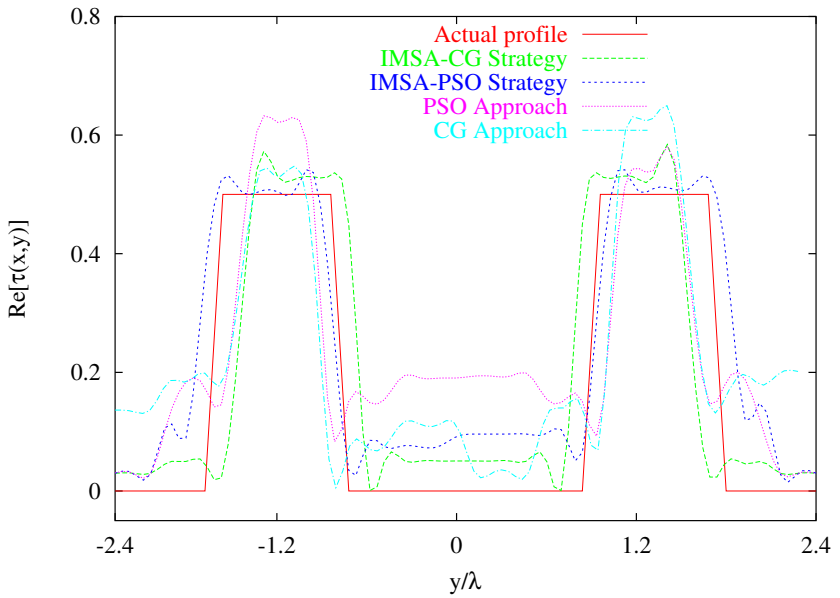

(b)

Fig. 3 - M. Donelli *et al.*, "A computational approach based on ..."

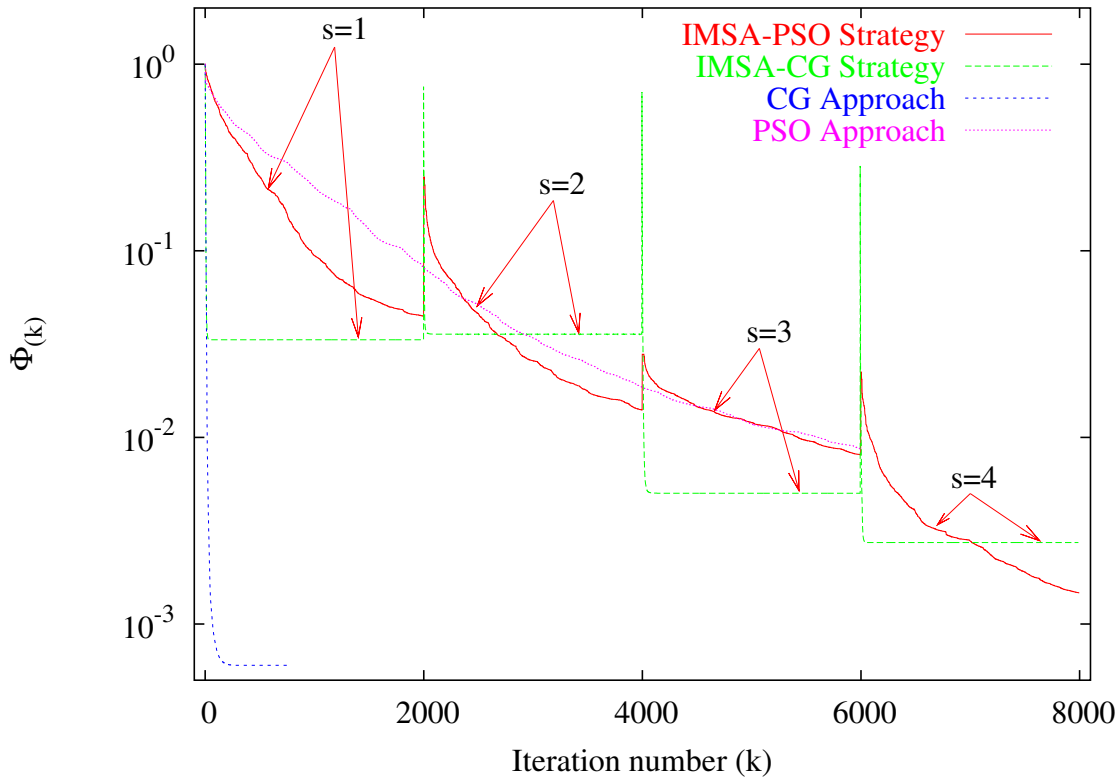

Fig. 4 - M. Donelli *et al.*, "A computational approach based on ..."

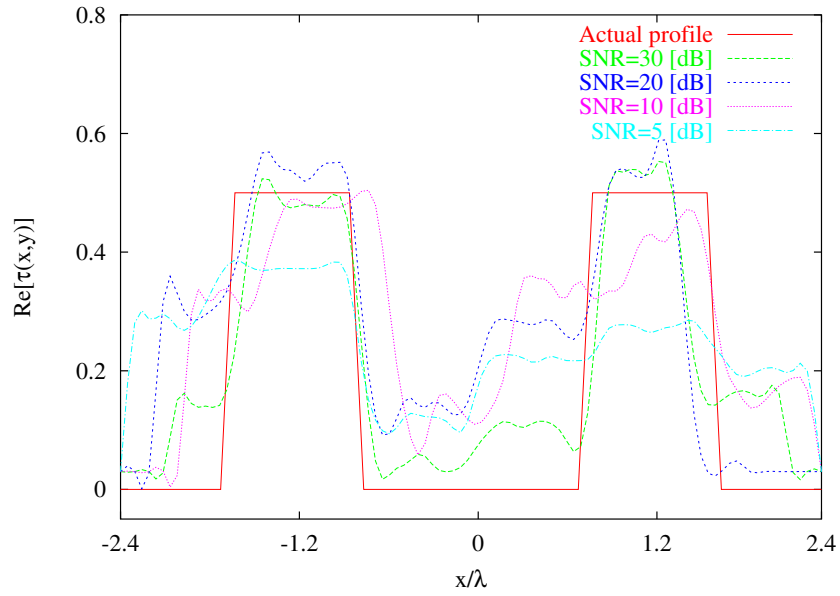

(a)

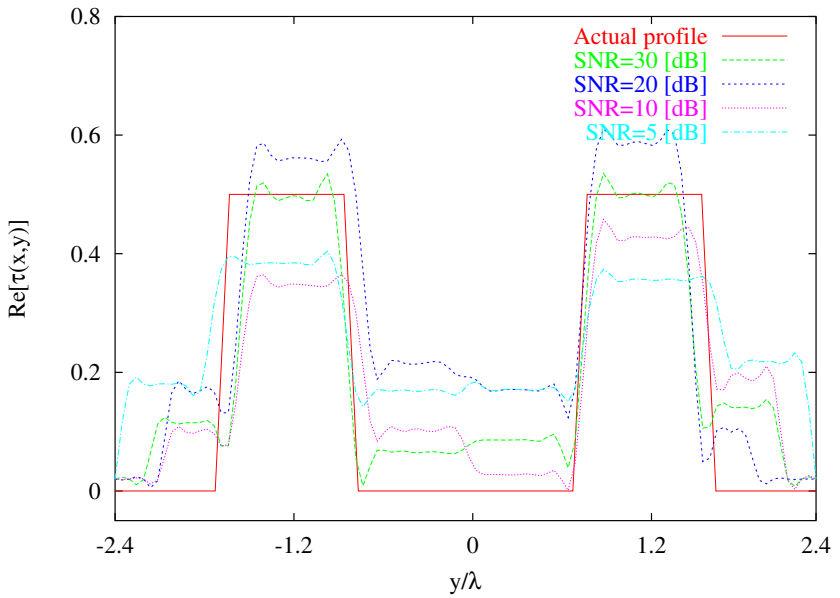

(b)

Fig. 5 - M. Donelli *et al.*, "A computational approach based on ..."

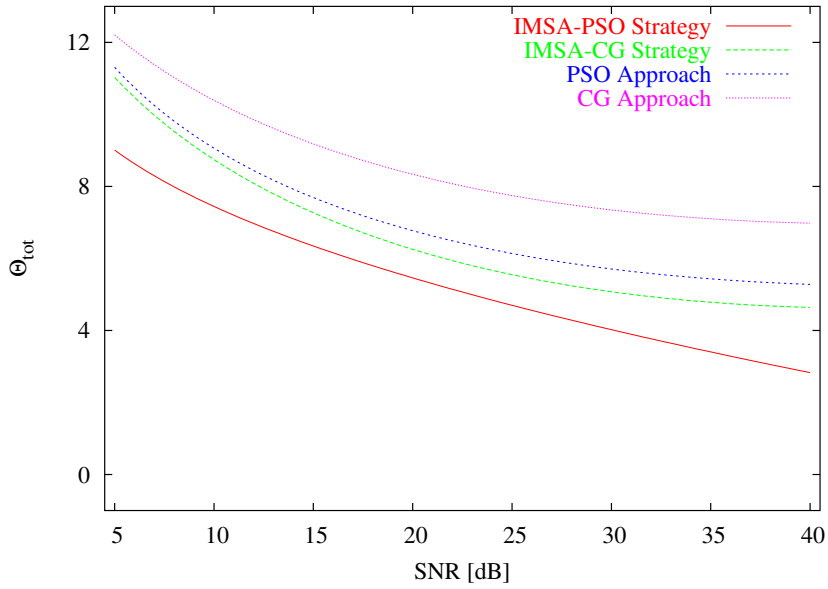

(a)

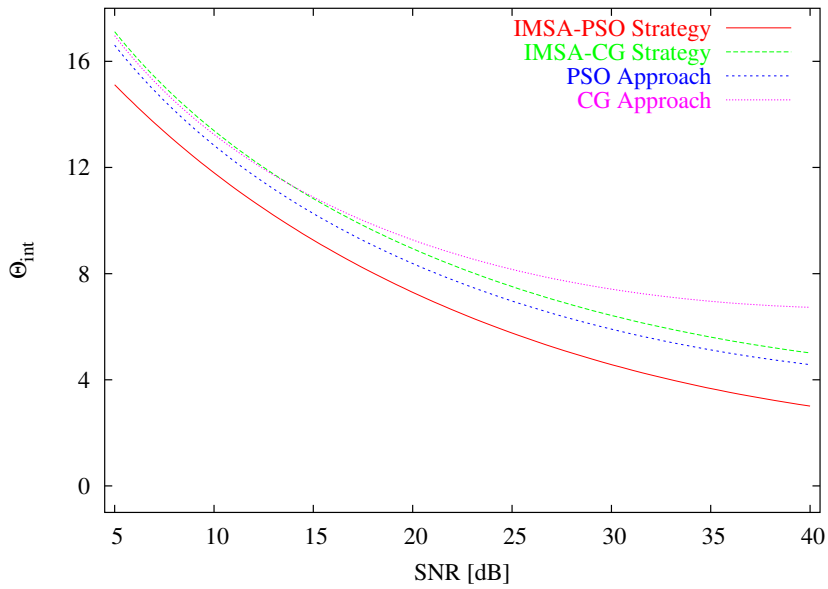

(b)

Fig. 6(I) - M. Donelli *et al.*, "A computational approach based on ..."

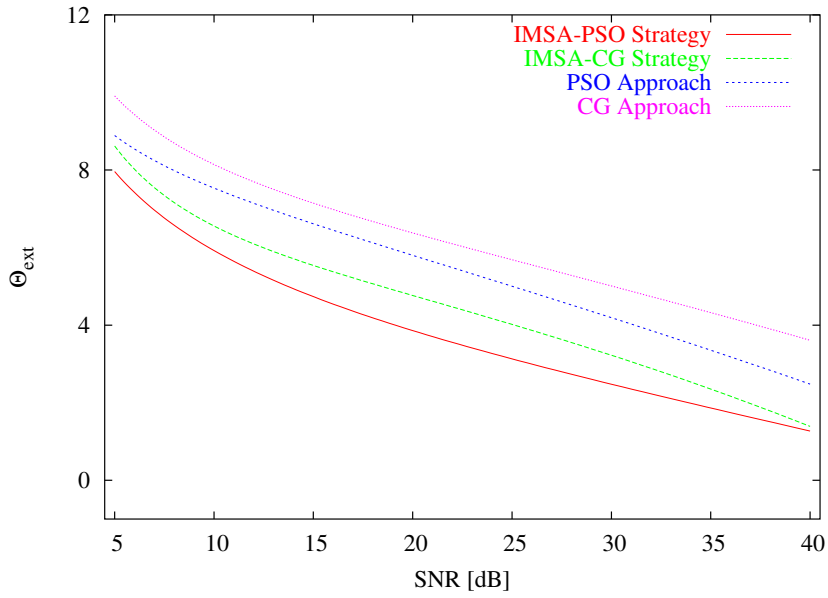

(c)

Fig. 6(*II*) - M. Donelli *et al.*, "A computational approach based on ..."

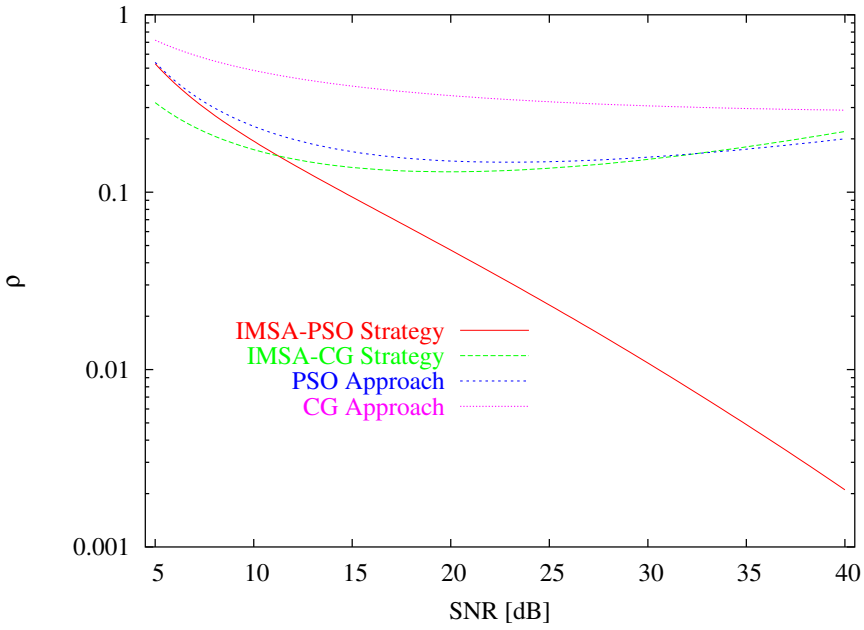

(d)

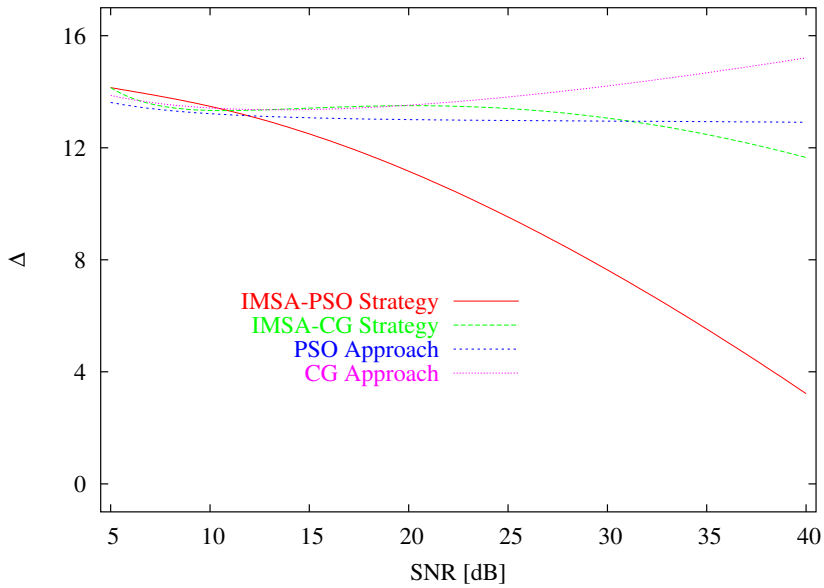

(e)

Fig. 6(*III*) - M. Donelli *et al.*, "A computational approach based on ..."

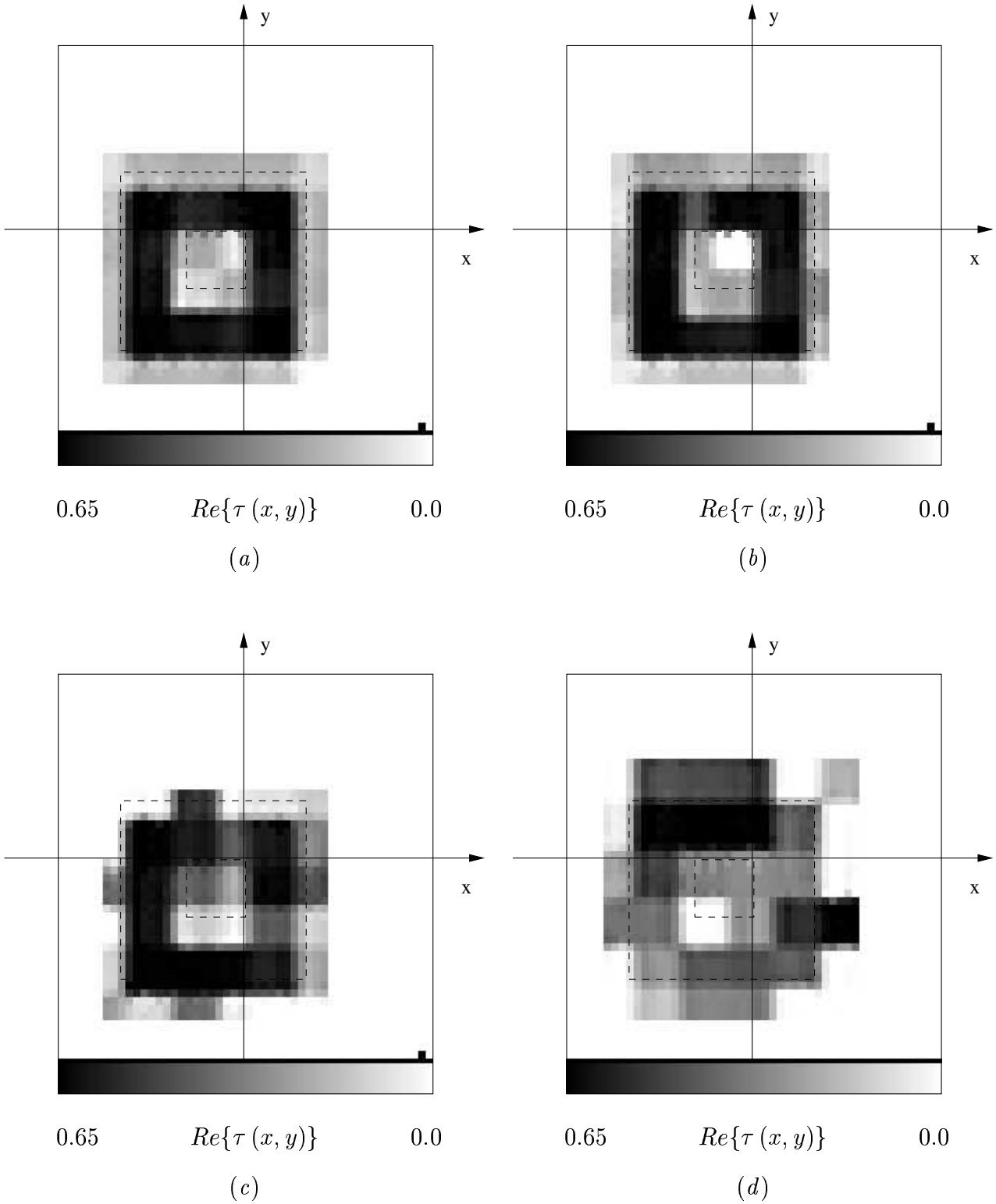

Fig. 7(*I*) - M. Donelli *et al.*, "A computational approach based on ..."

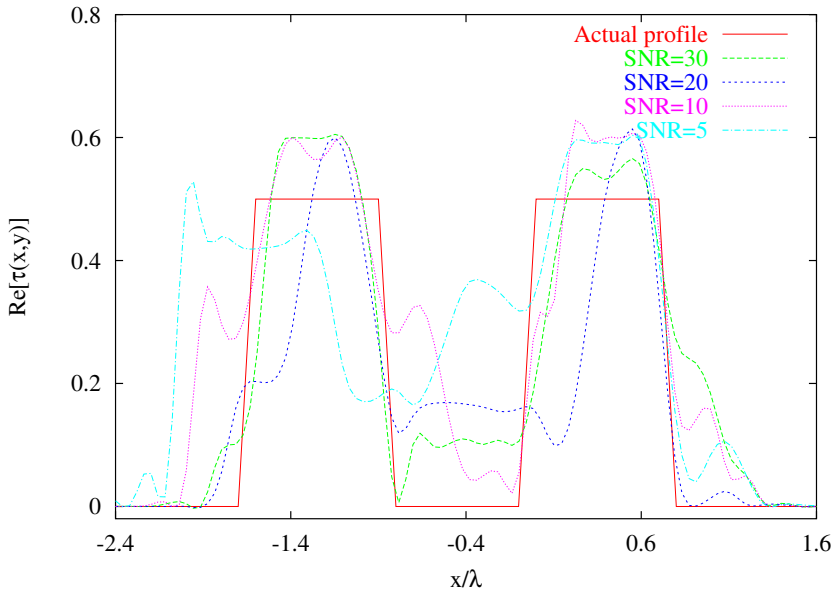

(e)

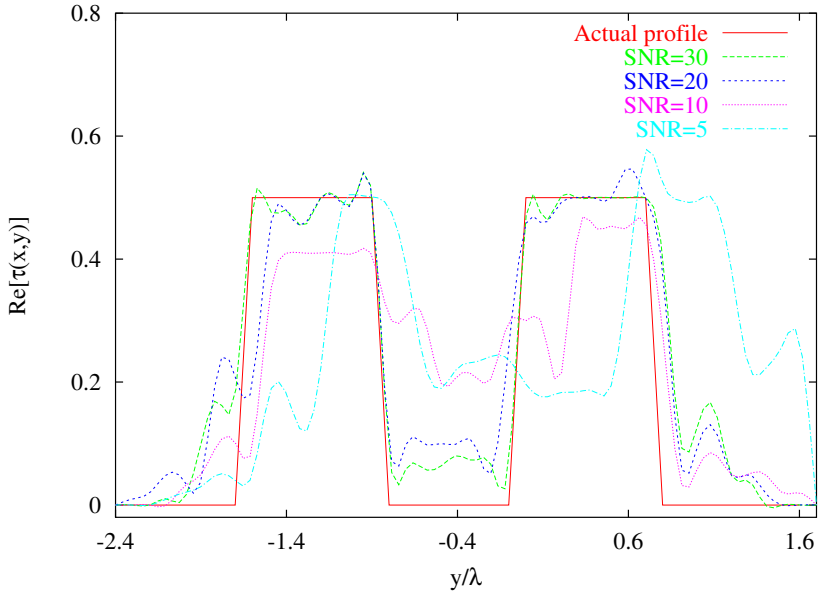

(f)

Fig. 7(*II*) - M. Donelli *et al.*, "A computational approach based on ..."

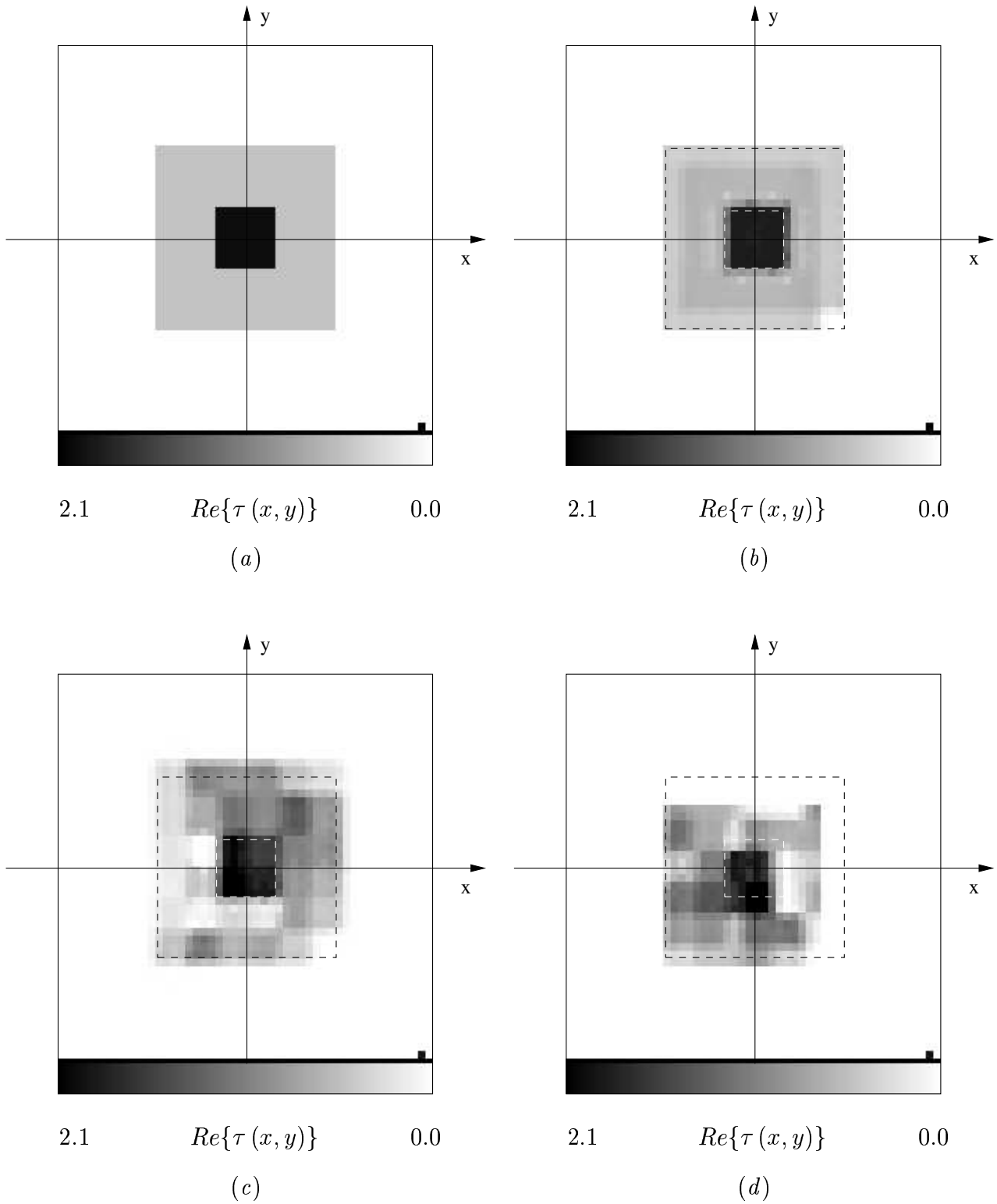

Fig. 8(I) - M. Donelli *et al.*, "A computational approach based on ..."

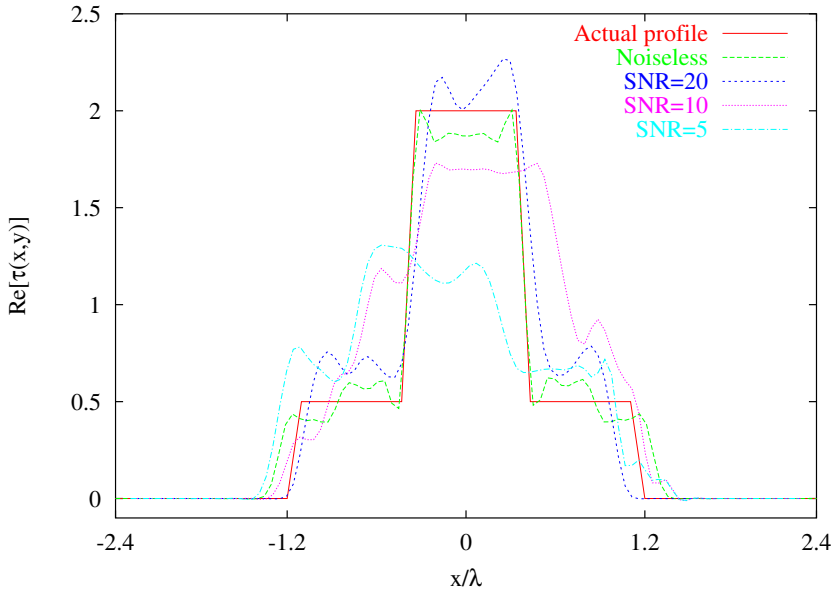

(e)

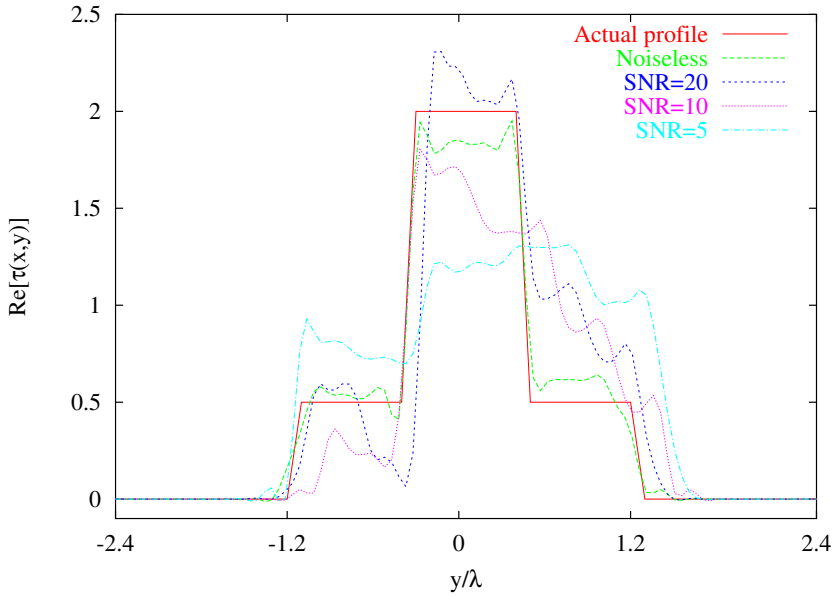

(f)

Fig. 8(*II*) - M. Donelli *et al.*, "A computational approach based on ..."

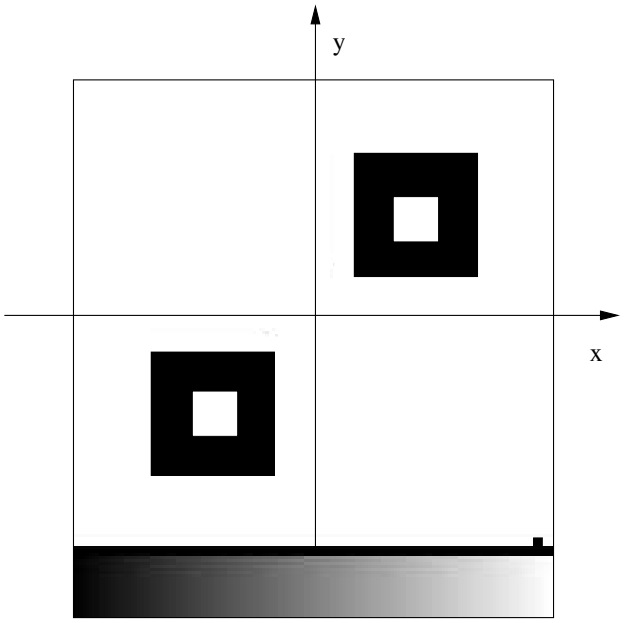

0.65 $Re\{\tau\,(x,y)\}$ 0.0

(a)

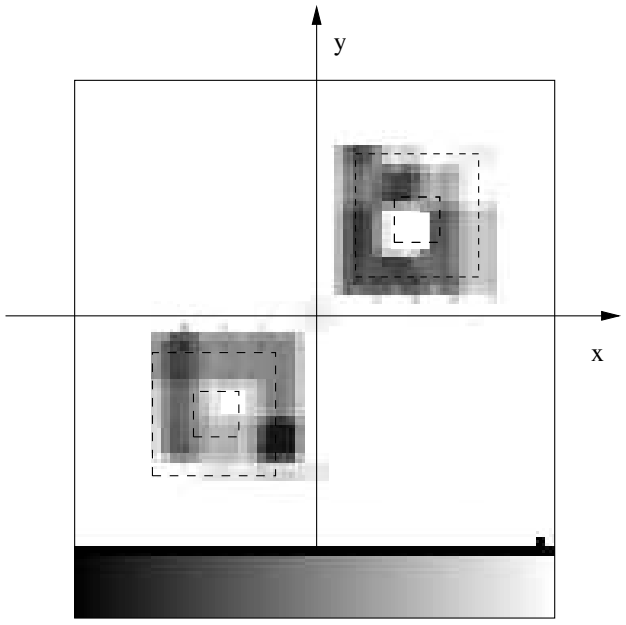

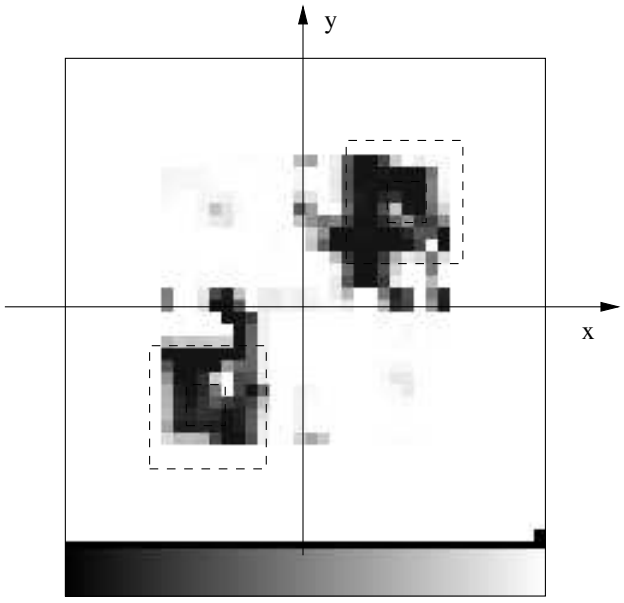

0.65 $Re\{\tau\,(x,y)\}$ 0.0 0.65 $Re\{\tau\,(x,y)\}$ 0.0

(b) (c)

Fig. 9 - M. Donelli *et al.*, "A computational approach based on ..."

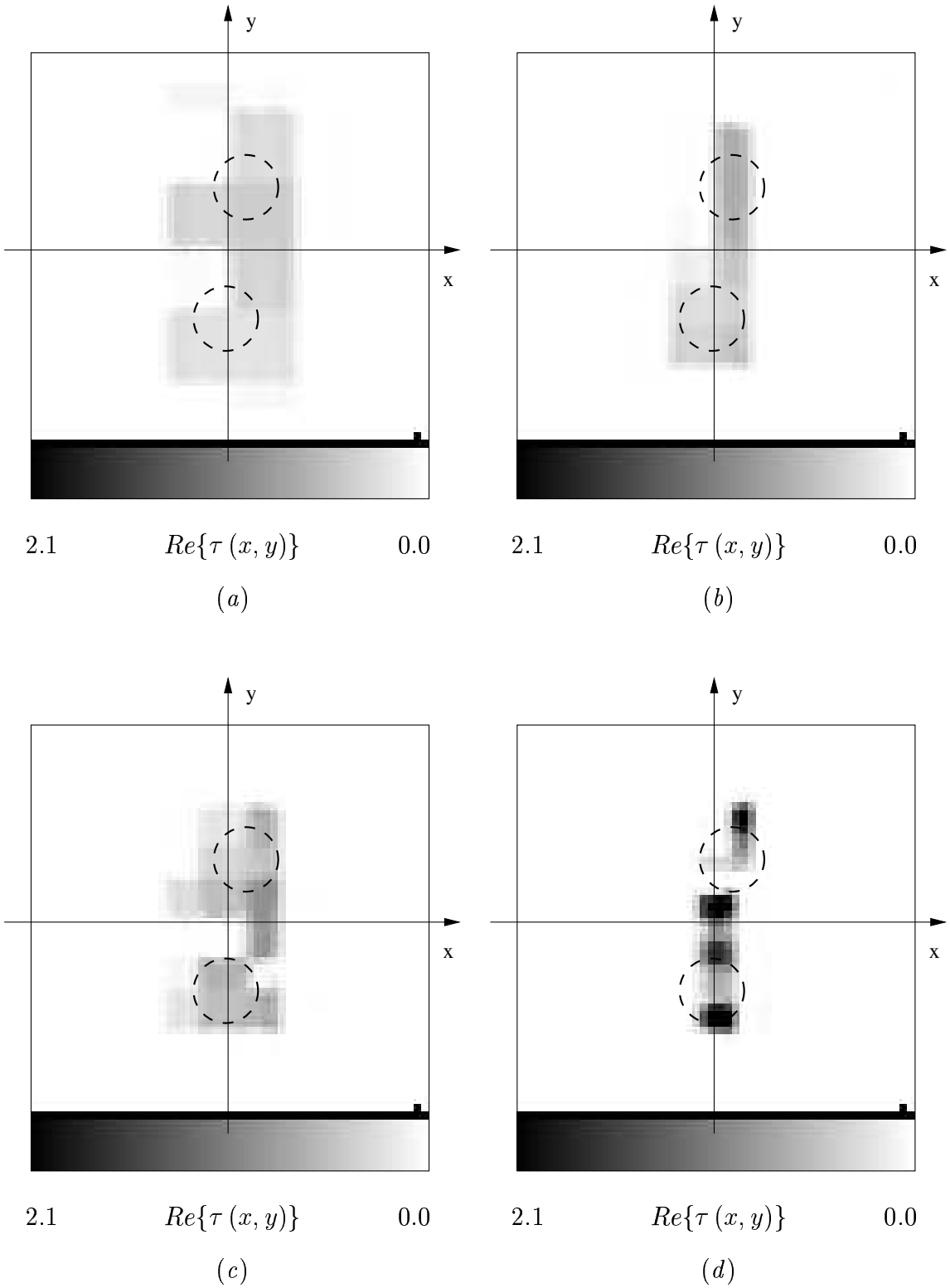

Fig. 10(I) - M. Donelli *et al.*, "A computational approach based on ..."

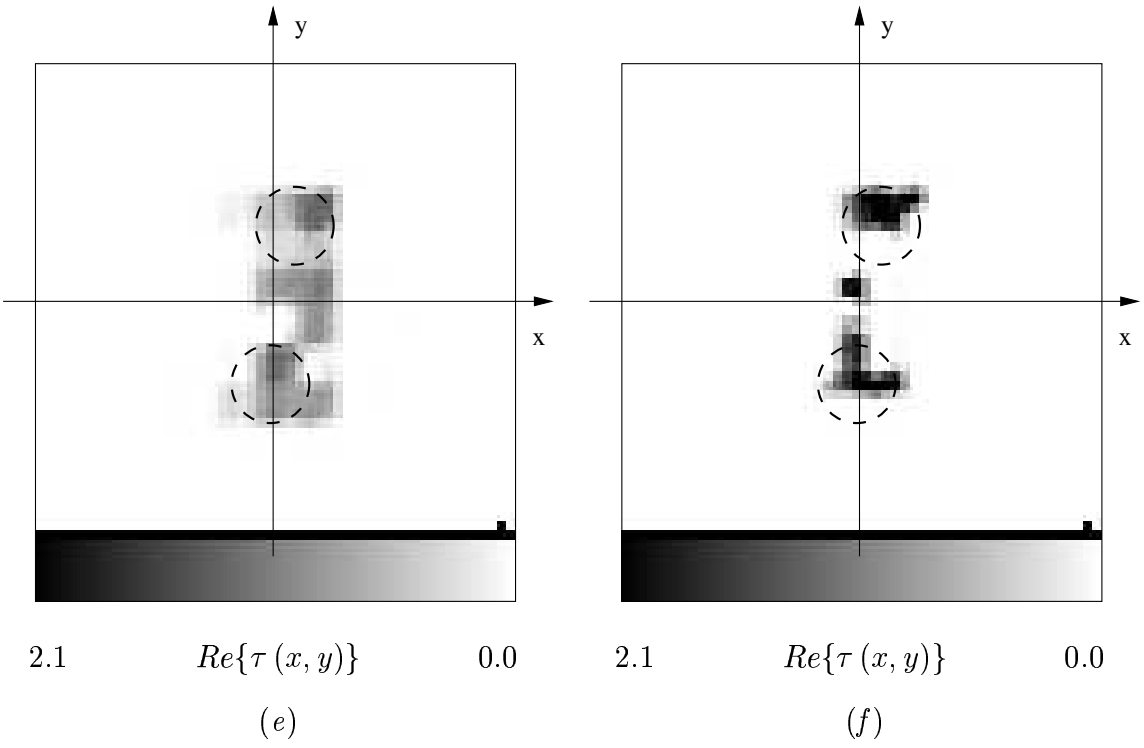

2.1 $Re\{\tau\,(x,y)\}$ 0.0

(e)

2.1 $Re\{\tau\,(x,y)\}$ 0.0

(f)

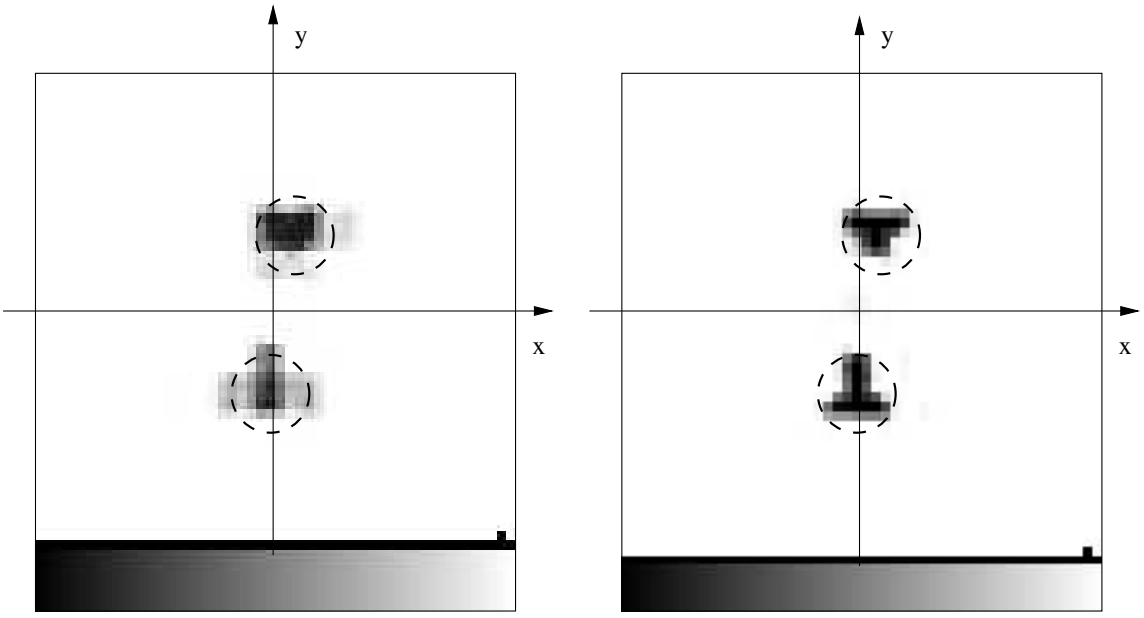

2.1 $Re\{\tau\,(x,y)\}$ 0.0

(g)

2.1 $Re\{\tau\,(x,y)\}$ 0.0

(h)

Fig. 10(*II*) - M. Donelli *et al.*, "A computational approach based on ..."

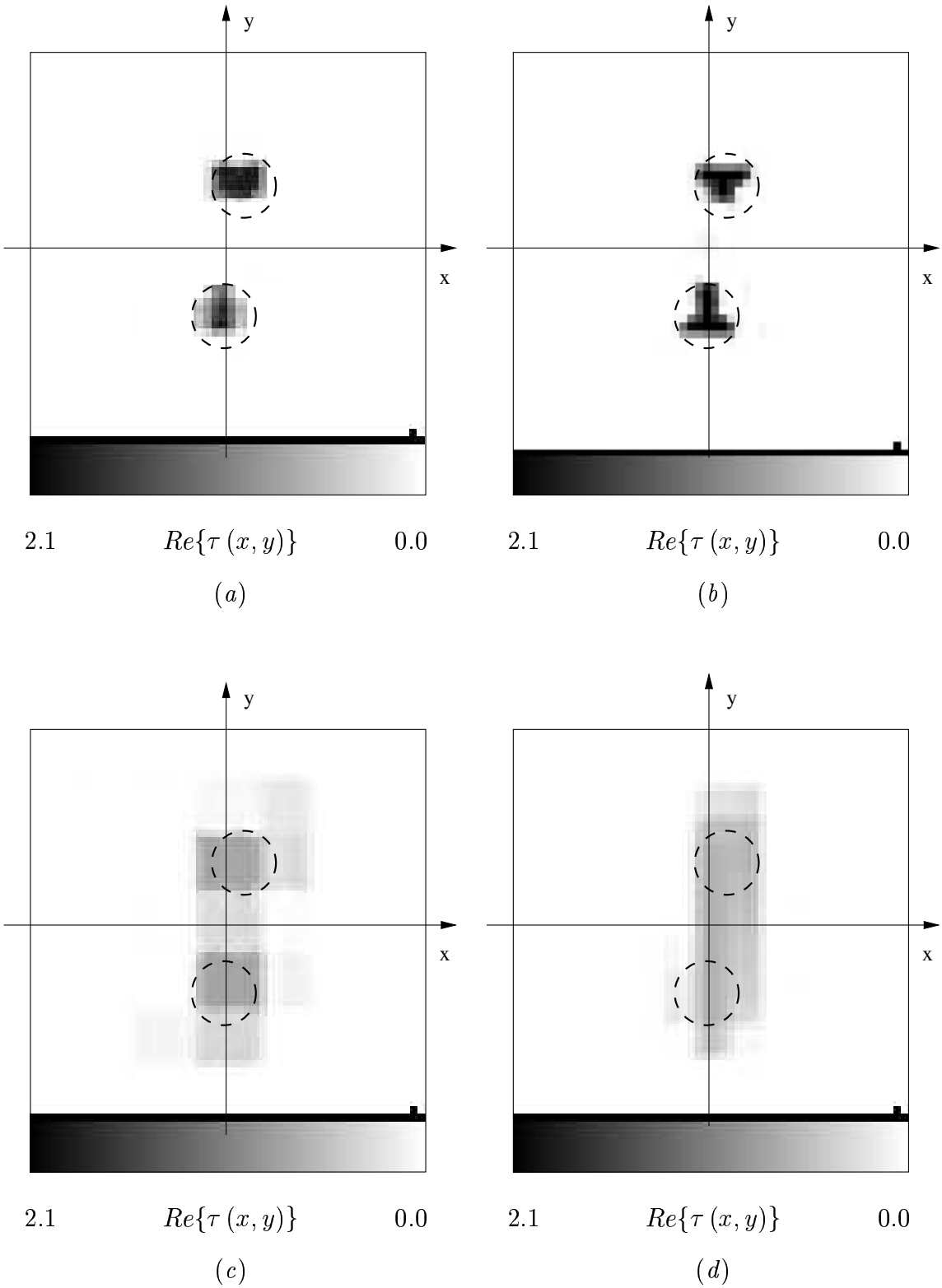

Fig. 11 - M. Donelli *et al.*, "A computational approach based on ..."

	$IMSA-PSO$					$IMSA-CG$				
Step No.	Θ_{tot}	Θ_{int}	Θ_{ext}	ρ	Δ	Θ_{tot}	Θ_{int}	Θ_{ext}	ρ	Δ
1	5.29	7.02	3.27	2.9×10^{-1}	15.02	7.59	15.91	5.59	5.9×10^{-1}	22.02
2	3.98	5.12	2.01	1.6×10^{-1}	14.01	6.98	9.81	4.32	1.9×10^{-1}	15.01
3	3.91	4.42	1.93	5.7×10^{-2}	7.73	5.39	6.78	2.98	2.0×10^{-1}	13.90
4	3.83	3.01	1.77	2.1×10^{-3}	3.22	4.64	5.01	1.39	2.2×10^{-1}	11.65

Tab. I - M. Donelli *et al.*, "An Integrated Multi-Scaling Strategy based on ..."

	$IMSA-PSO$	$IMSA-CG$	PSO	CG
Θ_{tot}	3.83	4.64	5.28	6.98
Θ_{int}	3.01	5.01	4.57	6.73
Θ_{ext}	1.77	1.39	2.48	3.61
ρ	2.1×10^{-3}	2.2×10^{-1}	1.9×10^{-1}	2.8×10^{-1}
Δ	3.22	11.65	12.91	15.21

Tab. II - M. Donelli *et al.*, "An Integrated Multi-Scaling Strategy based on ..."

	$IMSA-PSO$	$IMSA-CG$	PSO	CG
U [2]	360	360	500	500
K_{tot}	8000	8000	6000	771
S_{opt}	4	4	–	–
T_k [3]	8.2×10^{-2}	5.5×10^{-2}	1.26×10^{-1}	1.01×10^{-1}

Tab. III - M. Donelli *et al.*, "An Integrated Multi-Scaling Strategy based on ..."

[2] When the *IMSA* is used then N stands for the number of discretizations of the RoI ($N = N(R)$).
[3] Concerning the *IMSA* Strategy $U = 360$. For the *PSO* and *CG*-based Approaches $U = 500$.

SNR $[dB]$	Θ_{tot}	Θ_{int}	Θ_{ext}	ρ	Δ
30	4.42	6.82	1.66	4.1×10^{-2}	7.12
20	5.05	3.21	2.15	4.8×10^{-2}	9.88
10	5.89	8.23	3.89	2.7×10^{-2}	9.25
5	6.95	13.22	5.46	2.3×10^{-1}	13.51

Tab. IV - M. Donelli *et al.*, "An Integrated Multi-Scaling Strategy based on ..."

SNR $[dB]$	Θ_{tot}	Θ_{int}	Θ_{ext}	ρ	Δ
∞	3.38	4.78	0.01	1.8×10^{-3}	4.82
20	5.05	6.07	0.99	3.6×10^{-3}	7.40
10	6.54	13.10	1.59	1.0×10^{-1}	13.50
5	9.46	19.12	3.29	1.3×10^{-1}	14.15

Tab. V - M. Donelli *et al.*, "An Integrated Multi-Scaling Strategy based on ..."

	$IMSA-PSO$	$IMSA-CG$
Θ_{tot}	1.02	1.41
$\Theta_{int}\rfloor_{q=1}$	4.21	8.71
$\Theta_{int}\rfloor_{q=2}$	3.16	8.26
Θ_{ext}	0.42	0.53
$\rho\rfloor_{q=1}$	2.4×10^{-2}	5.0×10^{-2}
$\rho\rfloor_{q=2}$	1.3×10^{-2}	2.5×10^{-2}
$\Delta\rfloor_{q=1}$	11.04	31.04
$\Delta\rfloor_{q=2}$	9.24	31.24

Tab. VI - M. Donelli *et al.*, "An Integrated Multi-Scaling Strategy based on ..."